Mon. Not. R. Astron. Soc. **351,** 1290–1306 (2004) doi:10.1111/j.1365-2966.2004.07868.x

The European Large-Area *ISO* Survey (ELAIS): the final band-merged catalogue

M. Rowan-Robinson,[1⋆] C. Lari,[2] I. Perez-Fournon,[3] E. A. Gonzalez-Solares,[4] F. La Franca,[5] M. Vaccari,[6] S. Oliver,[7] C. Gruppioni,[8] P. Ciliegi,[8] P. Héraudeau,[9] S. Serjeant,[10] A. Efstathiou,[11] T. Babbedge,[1] I. Matute,[5] F. Pozzi,[8] A. Franceschini,[6] P. Vaisanen,[12,36] A. Afonso-Luis,[3] D. M. Alexander,[4] O. Almaini,[13] A. C. Baker,[19] S. Basilakos,[17] M. Barden,[22] C. del Burgo,[33] I. Bellas-Velidis,[17] F. Cabrera-Guerra,[3] R. Carballo,[18] C. J. Cesarsky,[14] D. L. Clements,[1] H. Crockett,[1] L. Danese,[20] A. Dapergolas,[17] B. Drolias,[1] N. Eaton,[1] E. Egami,[21] D. Elbaz,[19] D. Fadda,[10] M. Fox,[1] R. Genzel,[16] P. Goldschmidt,[1] J. I. Gonzalez-Serrano,[15] M. Graham,[1] G. L. Granato,[6] E. Hatziminaoglou,[3] U. Herbstmeier,[22] M. Joshi,[1] E. Kontizas,[17] M. Kontizas,[23] J. K. Kotilainen,[24] D. Kunze,[16] A. Lawrence,[13] D. Lemke,[22] M. J. D. Linden-Vørnle,[25,26] R. G. Mann,[13] I. Márquez,[27] J. Masegosa,[27] R. G. McMahon,[4] G. Miley,[28] V. Missoulis,[1] B. Mobasher,[29] T. Morel,[35] H. Nørgaard-Nielsen,[26] A. Omont,[31] P. Papadopoulos,[28] J.-L. Puget,[31] D. Rigopoulou,[34] B. Rocca-Volmerange,[30] N. Sedgwick,[10] L. Silva,[10] T. Sumner,[1] C. Surace,[1] B. Vila-Vilaro,[21] P. van der Werf,[28] A. Verma,[16] L. Vigroux,[19] M. Villar-Martin,[30,37] C. J. Willott,[32] A. Carramiñana[38] and R. Mujica[38]

[1]*Astrophysics Group, Blackett Laboratory, Imperial College, Prince Consort Rd, London SW7 2BZ*
[2]*Istituto di Radioastronomia, Via P. Gobetti 101, Bologna 40129, Italy*
[3]*Instituto de Astrofisica de Canarias, C/Via Lactea 38200 La Laguna, S/C de Tenerife, Spain*
[4]*Institute of Astronomy, Madingley Road, Cambridge, CB3 0HA*
[5]*Dipartimento di Fisica Universita degli Studi 'Roma TRE', Via della Vasca Navale 84, I-00146, Roma, Italy*
[6]*Dipartimento di Astronomia, Universita' di Padova, Vicolo Osservatorio 5, I-35122 Padova, Italy*
[7]*Astronomy Centre, Department of Physics & Astronomy, University of Sussex, Brighton BN1 9QJ*
[8]*Osservatorio Astronomico di Bologna, via Ranzani 1, 40127 Bologna, Italy*
[9]*Kapteyn Astronomical Institute, Postbus 800, 9700 AV Groningen, the Netherlands*
[10]*Centre for Astrophysics and Planetary Science, School of Physical Sciences, University of Kent, Canterbury, Kent CT2 7HR*
[11]*Department of Computer Science and Engineering, Cyprus College, 6 Diogenes St, Engomi, 1516 Nicosia, Cyprus*
[12]*European Southern Observatory, Casilla 19001, Santiago, Chile*
[13]*Institute for Astronomy, University of Edinburgh, Royal Observatory, Blackford Hill, Edinburgh EH9 3HJ*
[14]*ESO, Karl-Schwarzschild-Str 2, D-85748 Garching bei Munchen, Germany*
[15]*Instituto de Física de Cantabria (Consejo Superior de Investigaciones Científicas - Universidad de Cantabria), 39005 Santander, Spain*
[16]*Max-Planck-Institut für Extraterrestrische Physik, Postfach 1603, 85740 Garching, Germany*
[17]*National Observatory of Athens, Astronomical Institute, PO Box 20048, GR-11810, Greece*
[18]*Department de Matematica Aplicada, Universidad de Cantabria, 39005 Santander, Spain*
[19]*CEA/SACLAY, 91191 Gif sur Yvette cedex, France*
[20]*SISSA, International School for Advanced Studies, Via Beirut 2-4, 34014 Trieste, Italy*
[21]*Steward Observatory, University of Arizona, 933 North Cherry Avenue, Tucson, AZ 85721-0065*
[22]*Max-Planck-Institut für Astronomie, Königstuhl (MPIA) 17, D-69117, Heidelburg, Germany*
[23]*Section of Astrophysics, Astronomy & Mechanics, Department of Physics, University of Athens, Panepistimiopolis, GR-15783, Zografos, Greece*
[24]*Tuorla Observatory, University of Turku, Väisäläntie 20, FIN-21500 Piikkiö, Finland*
[25]*Niels Bohr Institute for Astronomy, Physics and Geophysics, Astronomical Observatory, Juliane Maries Vej 30, DK–2100 Copenhagen Ø, Denmark*
[26]*Danish Space Research Institute, Juliane Maries Vej 30, DK–2100 Copenhagen Ø, Denmark*
[27]*Instituto de Astrofísica de Andalucía, CSIC, Apartado 3004, E-18080 Granada, Spain*
[28]*Leiden Observatory, PO Box 9513, NL-2300 RA Leiden, the Netherlands*
[29]*Space Telescope Science Institute, Baltimore, FA, USA*
[30]*Institut d'Astrophysique de Paris, 98bis Boulevard Arago, F 75014 Paris, France*

⋆E-mail: m.rrobinson@imperial.ac.uk

[31]*Institut d'Astrophysique Spatiale (IAS), Bâtiment 121, Université Paris XI, 91405 Orsay cedex, France*
[32]*Herzberg Institute of Astrophysics, National Research Council, 5071 West Saanich Rd, Victoria, BC V9E 2E7, Canada*
[33]*ESTEC, Keplerlaan 1, Postbus 299, 2200 AG Nordwijk, the Netherlands*
[34]*Physics Department, University of Oxford, Denys Wilkinson Building, Keble Rd, Oxford OX1 3RH*
[35]*Istituto Nazionale di Astrofisica, Osservatorio Astronomico de Palermo G.S.Vaiana, Piazza del Parlamento 1, I-90134, Palermo, Italy*
[36]*Observatory, Tahtitorninmaki, FIN-00014 University of Helsinki, Finland*
[37]*Department of Physical Sciences, University of Hertfordshire, College Lane, Hatfield, Herts AL10 9AB*
[38]*INAOE, Luis Enrique Erro 1, Tonantzintla, Puebla, Mexico*

Accepted 2004 March 22. Received 2003 December 12; in original form 2003 August 16

ABSTRACT

We present the final band-merged European Large-Area *ISO* Survey (ELAIS) Catalogue at 6.7, 15, 90 and 175 μm, and the associated data at U, g', r', i', Z, J, H, K and 20 cm. The origin of the survey, infrared and radio observations, data-reduction and optical identifications are briefly reviewed, and a summary of the area covered and the completeness limit for each infrared band is given. A detailed discussion of the band-merging and optical association strategy is given. The total Catalogue consists of 3762 sources. 23 per cent of the 15-μm sources and 75 per cent of the 6.7-μm sources are stars. For extragalactic sources observed in three or more infrared bands, colour–colour diagrams are presented and discussed in terms of the contributing infrared populations. Spectral energy distributions (SEDs) are shown for selected sources and compared with cirrus, M82 and Arp220 starburst, and active galactic nuclei (AGN) dust torus models.

Spectroscopic redshifts are tabulated, where available. For the N1 and N2 areas, the Isaac Newton Telescope ugriz Wide Field Survey permits photometric redshifts to be estimated for galaxies and quasars. These agree well with the spectroscopic redshifts, within the uncertainty of the photometric method [$\sim$10 per cent in $(1 + z)$ for galaxies]. The redshift distribution is given for selected ELAIS bands and colour–redshift diagrams are discussed.

There is a high proportion of ultraluminous infrared galaxies ($\log_{10}$ of 1–1000 μm luminosity $L_{\rm ir} > 12.22$) in the ELAIS Catalogue (14 per cent of 15-μm galaxies with known z), many with Arp220-like SEDs. 10 per cent of the 15-μm sources are genuine optically blank fields to $r' = 24$: these must have very high infrared-to-optical ratios and probably have $z > 0.6$, so are high-luminosity dusty starbursts or Type 2 AGN. Nine hyperluminous infrared galaxies ($L_{\rm ir} > 13.22$) and nine extremely red objects (EROs) ($r - K > 6$) are found in the survey. The latter are interpreted as ultraluminous dusty infrared galaxies at $z \sim 1$. The large numbers of ultraluminous galaxies imply very strong evolution in the star formation rate between $z = 0$ and 1. There is also a surprisingly large population of luminous ($L_{\rm ir} > 11.5$), cool (cirrus-type SEDs) galaxies, with $L_{\rm ir} - L_{\rm opt} > 0$, implying $A_V > 1$.

Key words: stars: formation – galaxies: evolution – galaxies: starburst – cosmology: observations – infrared: galaxies.

1 INTRODUCTION

The European Large-Area *ISO* Survey (ELAIS) was originally proposed in response to the first *Infrared Space Observatory* (*ISO*) call for open time proposals in 1995 by M. Rowan-Robinson and 11 co-investigators from nine institutions (Rowan-Robinson et al. 1999). Subsequently the collaboration has grown to a total of 77 investigators from 32 European institutions. The original concept was for a survey of 12 deg^2 of sky at wavelengths of 15 and 90 μm. Subsequent awards of observing time allowed the survey to be extended to 6.7 μm and (in collaboration with the FIRBACK team led by J.-L. Puget) 175 μm. The ELAIS areas were also surveyed at 20 cm with the Very Large Array (VLA) and the Australia Telescope.

The survey goals, selection of survey areas, and details of the *ISO* observations were described by Oliver et al. (2000), and a preliminary analysis of the 6.7- and 15-μm data was reported by Serjeant et al. (2000) and of the 90-μm data by Efstathiou et al. (2000b). A new method of reduction of the 15-μm data, which incorporates physical models of cosmic ray and transient effects, was given by Lari et al. (2001), and a first application of this to the ELAIS S1

area was described by Gruppioni et al. (2001). The final 15-μm reduction of the S1 area is reported by Lari et al. (in preparation), of the S2 area by Pozzi et al. (2003) and of the N1, N2 and N3 areas by Vaccari et al. (2004) (see below for an explanation of survey areas). The final reduction of the 90-μm data is reported by Héraudeau et al. (2004) and of the FIRBACK–ELAIS 175-μm data by Dole et al. (2001). A future paper by Rodighiero et al. (in preparation) will report results of applying the Lari method to the ELAIS 90-μm data. The reduction and analysis of the 20-cm data was described by Ciliegi et al. (1999) for N1, N2 and N3, and by Gruppioni et al. (1999) for S1 and S2.

Associated with the ELAIS survey there has also been an extensive programme of ground-based optical and near-infrared imaging and spectroscopy. The optical and spectroscopic follow-up of the S1 area has been presented by La Franca et al. (2004), of the S2 area by Pozzi et al. (2003), and of the N1 and N2 areas by Vaisanen et al. (2002), Afonso-Luis et al. (in preparation), Gonzalez-Solares et al. (2004), Perez-Fournon et al. (in preparation), Serjeant et al. (2004) and Verma et al. (in preparation).

Deeper surveys at 6.7 and 15 μm were also carried out by a subset of the ELAIS consortium in the *Hubble Deep Field* North (HDF-N) (Goldschmidt et al. 1997; Mann et al. 1997; Oliver et al. 1997; Rowan-Robinson et al. 1997; Serjeant et al. 1997) and in HDF-S (Mann et al. 2002; Oliver et al. 2002).

X-ray surveys have also been carried out in several ELAIS areas. Alexander et al. (2001) reported *Beppo-Sax* observations over a large fraction of S1. Manners et al. (2003) have reported *Chandra* observations in the central regions of N1 and N2, and some interpretation of these observations has been given by Willott et al. (2003). *ROSAT* data were compared with the ELAIS Preliminary Catalogue by Basilakos et al. (2002).

The present paper reviews the parameters of the ELAIS survey, gives a detailed account of the merging of the different individual wavelength surveys to generate a final catalogue, and discusses the populations present in the survey through colour–colour and colour–redshift diagrams, and spectral energy distributions.

2 QUALITY OF THE CONSTITUENT INFRARED CATALOGUES

The separate wavebands making up the ELAIS survey each comprise an independent survey and are discussed in separate papers. The present paper does not replace these analyses but pulls together those aspects which emerge from band-merging the surveys. For detailed discussion and analysis of the ELAIS sources, it is essential to refer back to these analyses of the individual constituent surveys. Table 1 defines the survey areas, wavelengths, characteristic depth and source-densities.

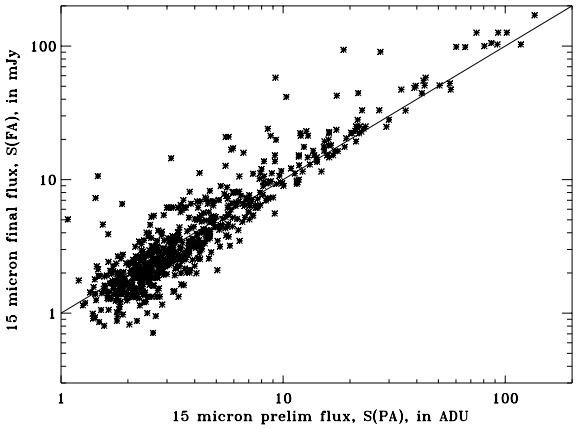

Figure 1. Comparison of Final Analysis 15-μm flux (mJy) (Lari et al., in preparation; Vaccari et al., in preparation) with Preliminary Analysis 15-μm fluxes (ADU) (Serjeant et al. 2000). The line corresponds to equal fluxes.

The calibration, completeness and reliability of the ELAIS 15-μm survey final analysis has been discussed by Lari et al. (2001), Gruppioni et al. (2001) and Vaccari et al. (2003). In the Lari method (Lari et al. 2001), the ISOCAM Handbook (Blommaert et al. 1998) conversion factor from *ISO* instrumental units (ADU) to mJy of 1.96 is used, with full modelling of the detector stabilization. To achieve consistency with the *IRAS* Faint Source Catalog 12-μm calibration a multiplicative factor of 1.097 is applied to 15-μm fluxes, based on the analysis by Aussel & Alexander (in preparation) of near-infrared, *ISO* and *IRAS* fluxes for stars (Vaccari et al. 2004). The *IRAS* 12-μm calibration has been tested by Aussel and Alexander for over 4000 stars detected by *IRAS* and by 2MASS. By contrast, the preliminary analysis (PA) of Serjeant et al. (2000) used a direct conversion of 1.75 ADU/mJy, based on a comparison of *ISO* and *IRAS* fluxes for stars, without correction for detector stabilization. Subsequently Vaisanen et al. (2002) used *J* and *K* observations of *ISO* stars to derive a corrected conversion factor for the PA Catalogue of 1.05 ADU mJy^{-1}. Fig. 1 shows a plot of the final 15-μm flux, S_{15}, versus the PA flux (in ADU) (Babbedge 2004), which supports the conclusions of Vaisanen et al. (2002). The Final Analysis Catalogue goes significantly deeper than the PA Catalogue, but almost all PA sources are found to be real, though much of the scatter in Fig. 1 must be attributed to lower accuracy of the PA fluxes.

It would also have been desirable to apply the Lari method to the 6.7-μm survey, but we have not been able to put together the very considerable resources needed to do this. As we will see in Section 3.3, 75 per cent of the 6.7-μm sources are stars, so the scientific returns for the present, predominantly extragalactic, study

Table 1. Summary of survey wavelengths, areas and numbers of sources, characteristic depth and source densities.

Name	RA	Dec	6.7	15	90	175 μm
N1	$16^h\ 10^m\ 01^s$	$+54^\circ\ 30'\ 36''$		2.67/490	2.56/151	2/103 (deg^2/no. of sources)
N2	$16^h\ 36^m\ 58^s$	$+41^\circ\ 15'\ 43''$	2.67/628	2.67/566	2.67/174	1/55
N3	$14^h\ 29^m\ 06^s$	$+33^\circ\ 06'\ 00''$	1.32/189	0.88/131	1.76/119	
S1	$00^h\ 34^m\ 44^s$	$-43^\circ\ 28'\ 12''$	1.76/304	3.96/317	3.96/226	
S2	$05^h\ 02^m\ 24^s$	$-30^\circ\ 35'\ 55''$	0.12/40	0.12/43	0.11/5	
	Total area/number		5.86/1161	10.3/1546	11.06/674	3.0/158 deg^2/no. of sources
	Characteristic depth		1.0	0.7	70	223 mJy
	Source-density		200	150	61	53 deg^{-2}

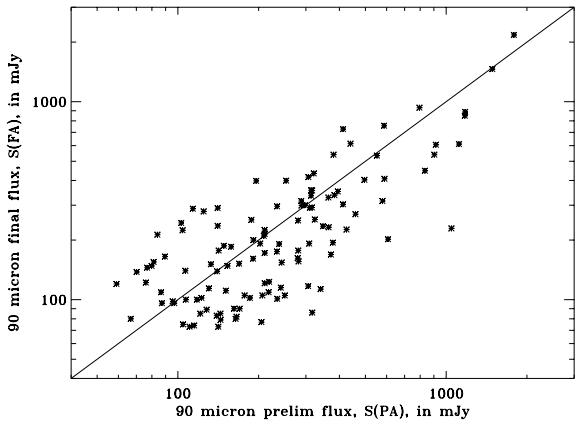

Figure 2. Comparison of Final Analysis 90-μm flux (mJy) (Héraudeau et al. 2004) with Preliminary Analysis 90-μm fluxes (Efstathiou et al. 2000b).

did not seem great. We have relied on the analysis of Vaisanen et al. (2002) which confirmed both the reality of the 6.7-μm Preliminary Analysis sources, and their flux calibration. The SIRTF–SWIRE survey (Lonsdale et al. 2003) will allow comparison of the 6.7-μm *ISO* fluxes with SIRTF 8-μm fluxes, for sources in N2 and S1. The 6.7-μm PA Catalogue has duplicate entries where different rasters observed the same part of the sky and only the entry with lowest noise was included.

The calibration, completeness and reliability of the ELAIS 90-μm survey final analysis has been discussed by Héraudeau et al. (2004). Calibration of 90-μm photometry is based on a direct comparison of standard stars. Fig. 2 shows a plot of the final 90-μm flux, S_{90}, versus the PA flux (Babbedge 2004). Again, most of the PA sources are confirmed. The substantial scatter can be mainly attributed to the limitations of the PA processing.

The 175-μm data analysis and identifications have been discussed by Dole et al. (2002). A 5-σ sensitivity of 223 mJy was achieved.

3 FINAL BAND-MERGED CATALOGUE

3.1 Band-merging

We have proceeded with the band-merging of the multiwavelength ELAIS catalogues in a sequential way, taking into account the different positional accuracies of the component catalogues. The 1-σ positional uncertainties at 15 μm and 20 cm have been estimated to be ∼1 arcsec (Ciliegi et al. 1999; Gruppioni et al. 1999; Gonzalez-Solares et al. 2004; Lari et al., in preparation; Vaccari et al., in preparation), so sources at these wavelengths can be very reliably associated with optical counterparts, down to at least $r' \sim 23$ mag. We therefore first separately identify the 15-μm and 20-cm catalogues with optical sources, using the likelihood method of Mann et al. (1997), as discussed by Gonzalez-Solares et al. (2004). The latter have described detailed simulations of this association process, which show that the probability of spurious associations is <5 per cent for $r' < 20$, rising to 20 per cent by $r' = 24$. The 15-μm and 20-cm sources are then merged on the basis of their optical positions, using a search radius of *2* arcsec. If the optical positions agree to this accuracy, the radio flux and error are added to the 15-μm catalogue entry. The percentages of 15-μm and 20-cm sources which found matches with the other wavelength were 8 per cent and 11 per cent, respectively. A flag is set for sources for which there is more than one candidate identification (see below): the selected association is the one with the highest likelihood (Gonzalez-Solares et al. 2004).

Radio sources which did not find a 15-μm match are then interleaved with the matched sources to give a right ascension (RA) ordered list. Matched sources are given the 15-μm source name.

We next matched the 6.7-μm PA sources with the combined 15-μm–20-cm list, using a search radius of 5 arcsec. The larger search radius is required because of the poorer astrometry of the PA Catalogue, which is based on a single raster, with pixel size 3 arcsec. 30 per cent of 6.7-μm sources found a match with a Catalogue source.

Non-matched 6.7-μm sources were associated with optical counterparts where possible, and then interleaved to generate a combined 6.7–15 μm 20-cm source-list. The positions of all sources in this list which did not have 20-cm fluxes were examined in the ELAIS 20-cm data to see whether a source in the 3–5 σ range might be present, and also in the VLA FIRST survey for areas not surveyed by ELAIS, and if so the flux was added to the Catalogue. Otherwise 3-σ radio limits are given as negative entries in the Catalogue.

The 90- and 175-μm sources were then associated with this combined list using search radii of 30 and 60 arcsec, respectively. Where a 90- or 175-μm source is matched with more than one Catalogue entry, the less probable associations are flagged and are not used in subsequent discussions of infrared colours or spectral energy distributions, i.e. all the flux is assigned to the most likely match. The non-matched 5-σ 90- and 175-μm sources are retained as a separate supplementary catalogue, because of their much poorer positions. They were searched for optical counterparts of high likelihood using search radii of 45 and 90 arcsec. Because of the large positional uncertainties at 90 and 175 μm, optical counterparts have to be reasonably bright to have a high likelihood of being the correct association ($r < 19.0$). 20 per cent of 90-μm sources and 1 per cent of 175-μm sources, brighter than 5σ, found matches neither with the combined 6-7-15 μm–20-cm source-list nor with optical counterparts. Most of these may be associated with galaxies fainter than $r' = 19$. However we cannot rule out the possibility that some of the unassociated 90-μm sources may be spurious.

Finally the combined 6.7-15-90-175 μm–20-cm Catalogue is searched for pairs within 5 arcsec and each of these is examined individually. In most, but not all, cases these pairs are believed to be the same object, split in two by the optical association process, and in these cases the sources have been merged, with an appropriate flag set in the Catalogue.

3.2 Catalogue description

The Final Band-merged Catalogue is given at http://astro.imperial.ac.uk/elais/. The Catalogue entries are: source name (for merged sources, in order of preference 15 μm, 20 cm, 6.7, 90, 175 μm), source position (same order of preference for merged sources), 20-cm flux and error, 175-μm flux, error, signal-to-noise ratio (S/N), positional offset, 90-μm flux, error, S/N, positional offset, 15-μm flux and S/N, 6.7-μm flux and error, 6.7-μm reliability flag (2 = high reliability, 3 = medium reliability), flag 1 (see below), flag 2, *J* mag and error, *H* mag and error, *K* mag and error, flag 3, position of optical association, Wide Field Survey (WFS) *U*, g', r', i', *Z* magnitudes and errors, WFS star/galaxy flags (−1 for stellar image, 1 for extended image), SExtractor r' mag and error, SExtractor star/galaxy classification (0.0 for galaxy, >0.7 for stellar image), positional offset of optical ID (total, RA, Dec), probability of optical association (threshold 0.8, see equation (5) of Gonzalez-Solares et al. 2004 for a definition), reliability of optical association (see equation 6 of Gonzalez-Solares

et al. 2004 for a definition), photometric spectral energy distribution (SED) type, $n_{\rm typ}$, and redshift ($\log_{10}(1 + z_{\rm phot})$, derived assuming $A_V = 0$), photometric SED type and redshift and A_V (free fit for A_V), spectroscopic redshift $z_{\rm spect}$, flag 4, flag 5, $z_{\rm best} = z_{\rm spect}$ if available, = $z_{\rm phot}$ otherwise, bolometric optical luminosity $L_{\rm opt}$, ir SED type (1 = cirr, 2 = M82-sb, 3 = A220-sb, 4 = active galactic nuclei (AGN) dust torus, 5 = cooler cirrus, 6 = 2 + 4), bolometric (1–1000 μm) infrared luminosity $L_{\rm ir}$, AGN dust torus luminosity $L_{\rm tor}$ (if 15-μm emission is interpreted as due to dust torus emission); where

(i) flag 1 = 1 if radio flux force-merged (15 μm and radio positions within *5* arcsec), = 2 if 6.7-μm flux force-merged, = 3 if 90-μm association is not the most likely, where there are multiple associations, = 4 if 175-μm association is not the most likely, where there are multiple associations, = 5 if second most probable optical association for 15 μm has been preferred on basis of radio position, = 6 if source has an *IRAS* association, = 7 if 1 and 6 both set, = 8 if 3 and 4 both set, = 9 if 1 and 8 both set, or 4 and 5 both set;

(ii) flag 2 = 1 if source falls in gaps between WFS chips, so no optical data, = 2 if the source falls near the edge of the WFS chip, so photometry may be unreliable, = 3 if source has multiple optical counterparts, = 4 if source is blank in optical (i.e. no optical counterpart with probability of association >0.7, within specified search radius), = 6 if there is an association in the NASA Extragalactic Data Base (NED) (non-ELAIS, non-2MASS, non-*IRAS*), = 7 if the association is a bright star, = 8 if flags 1 and 7 set, = 9 if flags 3 and 7 set;

(iii) flag 3 = 1 if *J*, *H*, *K* magnitudes from 2MASS, = 2 if *J*, *K* magnitudes from Vaisanen et al. (2002), = 3 if *K* magnitudes from Rigopoulou et al. (in preparation), = 4 if *K* magnitude from Pozzi et al. (2003) = 5 if *K* magnitude from Sajina et al. (2003);

(iv) flag 4, $n_{\rm ztyp}$ (spectroscopic classification), = 1 (spiral) galaxy, = 2 emission-line, starburst, = 3 absorption line, early type, = 4 AGN, = 5 Sy1, = 6 Sy2, = 7 star, = 8 liner;

(v) flag 5, $n_{\rm zref}$ = 1 Perez-Fournon et al. (2004), = 2 Serjeant et al. (2004), = 3 La Franca et al. (2004), = 4 Pozzi et al. (2003), = 5 NED, = 6 Morel et al. (2001), = 7 SLOAN Survey, = 8 Willott et al. (2003), = 9 Chapman et al. (2002), Sajina et al. (2003).

For extended objects in N1, N2, the WFS magnitudes refer to the flux within a fixed aperture: they should give the correct colours of the objects, as required by the photometric redshift code. For integrated magnitudes the SExtractor r' magnitude should be used (and other WFS bands can be corrected by the difference between the WFS and SExtractor r' magnitudes). Because of the effects of saturation, colours can only be trusted if the SExtractor r' magnitude is >15 (this mainly affects stars in the Catalogue). In S1, the *B* magnitudes are derived from Automatic Plate Measuring (APM) magnitudes and are very uncertain (also possibly too faint on average by ∼0.5 mag).

There are 3523 sources in the 6.7–15 μm–20-cm Catalogue, of which 1636 are 15-μm sources, 1136 are 20-cm (non-15-μm) sources, 741 are 6.7-μm (non-15-μm, non-20-cm) sources, and 239 sources are in the supplementary 90–175 μm catalogue. The numbers of 15-μm sources with redshifts are 204 in S1 (199 spectroscopic), 31 in S2 (22 spectroscopic), 10 in N3 (all spectroscopic), 309 in N1 (109 spectroscopic) and 355 in N2 (167 spectroscopic), 909 15-μm redshifts in all, and 1210 redshifts in the whole Catalogue (see below for a discussion of photometric redshifts). 97 per cent of 15-μm sources in N1 and N2 are accounted for as either stars, extragalactic sources with redshifts, or blank fields (8 and 11 per cent, respectively), and 93 per cent in S1 (the percentage of blank fields in S1 is higher, 20 per cent, because of the shallower optical survey). 48 per cent of the radio (non-15-μm) sources are blank fields (to $r' = 24$). 91 per cent of the 6.7-μm (non-15-μm or radio) sources in N1 are found to be stars.

3.3 Associations

We matched the whole Catalogue with the NASA Extragalactic Data Base (NED) and redshifts resulting from these associations are included in our Catalogue. We also specifically matched the Catalogue to the 2MASS *J*, *H*, *K* catalogues, finding matches for 30 per cent of our sources (with a higher success rate for the stars). A search radius of 5 arcsec was used, and in the few cases where sources appeared in both the 2MASS Extended and Point-Source Catalogues, the magnitudes from the Extended Catalogue were preferred. Here we discuss some more specific results from associations with known objects.

Table 2 lists the *ISO* and *IRAS* data for ELAIS sources which are associated with *IRAS* Faint Source Catalog sources (FSC, Moshir et al. 1992), with upper limits indicated as negative values. Of the 39 associations in N1 and N2, 12 are clearly stellar photospheres detected by *IRAS* at 12 μm (and occasionally at 25 μm) and the rest are nearby normal galaxies. For the galaxies detected by *IRAS* at 60 and 100 μm, we have interpolated to estimate a 90-μm flux and calculated $\log_{10} S(90)_{\rm IRAS}/S(90)_{\rm ISO}$. The mean value for 19 sources is 0.129 ± 0.022, suggesting that there are unresolved calibration issues between *IRAS* and *ISO*. However it should be noted that there is a tendency for the *IRAS* FSC to overestimate fluxes near the FSC threshold at 60 and 100 μm (Moshir et al. 1992). Since all the *IRAS* sources in Table 2 have S(100) < 3 Jy (and most have S(100) < 1 Jy), this would be sufficient to explain the discrepancy noted above.

The ELAIS N1 field was also partially observed with the Hα survey of Pascual et al. (2001). Since the infrared and Hα both trace star formation it was tempting to see if there were any sources in common. Using the Hα, far-infrared (FIR), star formation calibrations of Cram et al. (1998) we were able to estimate a mean Hα flux to FIR flux. Then using a starburst SED we were able to estimate the expected 15-μm flux for each of the Pascual et al. sources. With one exception the expected 15-μm fluxes all fell below the characteristic depth of the survey (0.7 mJy, Table 1). The exception was the source in their field a3 with ID 7227b at $16^{\rm h}\,05^{\rm m}\,46\overset{\rm s}{.}3$, $+54^\circ\,39'11\overset{''}{.}74$ with $m_I = 17.5$ and $m_{\rm H\alpha} = 17.0$. We estimate that this source should have had a 15-μm flux of 2.9 mJy. Neither this source nor any of the others were detected in our ELAIS Catalogue. A more detailed analysis of the expected dispersion in the Hα/FIR relation is required before we can assess whether these non-detections suggest that the mean relation needs to be revised.

The Canada–France–Hawaii Telescope blue grens quasar survey of Crampton et al. (1992) overlaps with the N2 field. 79 of their candidates fall within the ELAIS boundaries. 11 of these candidates are detected by ELAIS and are listed in Table 3.

Stars can be recognized in the Catalogue through (i) having flag 2 set to 7, (ii) having flag 4 set to 7, (iii) having low ratios of (S_{15}/S_r) or $(S_{6.7}/S_r)$, where S_r is the *r*-band flux in mJy. Almost all sources with $\log_{10}(S_{15}/S_r) < -0.5$, or $\log_{10}(S_{6.7}/S_r) < -0.2$, are stars. A total of 846 stars have been identified in this way in the Catalogue, comprising 22, 23 and 25 per cent of the 15-μm sources in N2, N1 and S1, respectively, and 75 per cent of 6.7-μm sources. In N1, 91 per cent of sources which are 6.7-μm (non-15-μm or 20-cm) sources are stars. The infrared fluxes are consistent with being photospheric emission in almost all cases. The small number of stars where the

Table 2. Matches with the *IRAS* Faint Source Catalog Version 2.

IRAS name	12 (mJy)	25	60	100 μm	*IRAS–ISO* sepn (arcmin)	ELAIS name	6.7 (mJy)	15	90	175 μm
F00279−4253	−75.4	−76.4	649.0	1440.0	0.70	ELAISC15-J003022−423657	–	25.21	849	–
F00302−4249	−112.0	−99.0	232.0	−525.0	0.53	ELAISC15-J003244−423313	–	11.64	191	–
F00315−4421	178.0	−93.8	−123.0	−376.0	0.43	ELAISC15-J003402−440442	–	109.34	–	–
F00320−4342	−65.8	−103.0	309.0	685.0	0.25	ELAISC15-J003429−432614	6.18	24.32	408	–
F00325−4313	−96.6	−75.5	322.0	906.0	0.13	ELAISC15-J003458−425733	–	15.83	534	–
F00341−4428	−129.0	−155.0	202.0	−676.0	0.78	ELAISC15-J003626−441140	5.80	13.61	290	–
F00353−4418	−53.4	−70.8	204.0	−559.0	0.20	ELAISC15-J003741−440226	–	1.36	210	–
F00360−4355	−124.0	−128.0	374.0	1280.0	0.27	ELAISC15-J003828−433848	10.14	46.58	682	–
F00362−4416	135.0	−149.0	−166.0	−279.0	0.12	ELAISC15-J003836−440029	–	27.48	–	–
F14262+3328	−60.2	−59.7	317.0	518.0	0.27	ELAISC15-J142823.4+331513	–	12.72	448	–
F14266+3336	−67.7	−98.9	452.0	999.0	0.32	ELAISC15-J142847.1+332315	–	19.02	540	–
F14292+3318	143.0	−116.0	−105.0	−316.0	0.18	ELAISC15-J143123.5+330517	258.75	62.91	–	–
F14292+3327	−68.4	94.9	694.0	983.0	0.13	ELAISC15-J143125.3+331348	6.93	28.95	933	–
F14304+3341	−68.1	−47.6	201.0	476.0	0.13	ELAISC15-J143234.9+332833	–	1.57	434	–
F16022+5450	−45.0	−65.7	159.0	−614.0	0.70	ELAISC15-J160322.8+544237	–	2.36	101	–
F16029+5506	−66.7	−67.0	296.0	507.0	0.09	ELAISC15-J160408.4+545812	–	8.77	315	–
F16046+5415	−83.2	78.8	604.0	798.0	0.25	ELAISC15-J160552.5+540650	–	30.09	756	838
F16063+5405	−69.3	−57.6	244.0	−742.0	0.16	ELAISC15-J160736.5+535731	–	19.15	230	597
F16070+5439	97.5	−50.4	−93.2	−308.0	0.12	ELAISC15-J160812.7+543141	–	53.25	–	–
F16083+5400	−48.3	−42.6	184.0	−720.0	0.11	ELAISC15-J160934.7+535220	–	1.99	215	309
F16091+5357	207.0	69.9	−102.0	−419.0	0.09	ELAISC15-J161019.3+534934	–	103.67	–	–
F16091+5447	576.0	146.0	−91.2 7	−244.0	0.02	ELAISC15-J161017.6+543929	–	288.39	–	–
F16145+5447	−35.7	−64.4	161.0	475.0	0.33	ELAISC15-J161545.8+544019	–	20.70	303	–
F16294+4115	−87.8	−65.4	243.0	936.0	0.13	ELAISC7-J163104+410913	2.96	–	540	–
F16298+4129	131.0	−53.5	−124.0	−424.0	0.22	ELAISC15-J163130.2+412330	255.16	66.21	–	–
F16323+4127	−74.9	−67.8	383.0	743.0	0.23	ELAISC15-J163401.8+412052	9.60	20.37	403	666
F16334+4116	−48.4	−65.0	190.0	−813.0	0.17	ELAISC15-J163506.1+411038	–	7.98	251	346
F16337+4101	−66.4	−73.7	224.0	−843.0	0.17	ELAISC15-J163525.1+405542	5.46	13.91	416	682
F16338+4138	147.0	−70.2	−104.0	−322.0	0.12	ELAISC15-J163531.1+413158	524.98	106.80	–	–
F16341+4053	103.0	−80.2	−88.2	−369.0	0.24	ELAISC15-J163549.0+404720	196.97	58.42	–	–
F16341+4059	243.0	−109.0	−102.0	−339.0	0.10	ELAISC15-J163549.9+405317	–	125.86	–	–
F16344+4111	−71.9	−67.6	351.0	897.0	0.06	ELAISC15-J163608.1+410507	2.30	8.94	614	803
F16349+4038	−84.7	−35.8	236.0	615.0	0.37	ELAISC15-J163633.5+403245	6.15	16.52	291	–
F16349+4034	116.0	−50.7	−98.7	−441.0	0.04	ELAISC15-J163637.3+402824	–	49.44	–	–
F16359+4058	−61.1	104.0	1220.0	2480.0	0.19	ELAISC15-J163734.4+405208	18.37	53.56	1461	2377
F16365+4202	−69.6	84.4	460.0	1500.0	0.28	ELAISC15-J163814.0+415620	6.14	50.15	611	–
F16377+4150	−54.3	−68.8	306.0	520.0	0.16	ELAISC15-J163924.0+414442	2.55	8.13	299	–
F16389+4146	249.0	81.2	−86.2	−500.0	0.06	ELAISC15-J164033.9+414107	645.30	125.86	–	–
F16405+4113	−55.6	−68.4	169.0	−545.0	0.15	ELAISC15-J164211.9+410816	1.80	8.32	288	–

ISO emission appears to be in excess of the photospheric prediction deserve further detailed study, but this is beyond the scope of the present paper.

4 RADIO–INFRARED–OPTICAL COLOUR–COLOUR DIAGRAMS

For sources detected in three bands we can plot colour–colour diagrams and compare the results with predictions of models. Figs 3–8 below show a selection of these, with predicted loci corresponding to the basic infrared templates used by Rowan-Robinson (2001): cirrus, M82 starburst, Arp220 starburst, AGN dust torus.

Fig. 3 shows the 175–90–15 colour–colour diagram for N1 and N2, with loci for cirrus (C), M82 starburst (S), and Arp220 starburst (A), for redshifts from 0 to 3 (the position of the labels indicates the zero-redshift end of the loci). The cross in the lower left-hand corner of this and subsequent diagrams indicates typical (median) error bars (where these are larger than the plotted symbols). The model loci loop around the diagram so without additional redshift information it is hard to say much about the populations (or derive photometric redshifts from far-infrared data). However, from both spectroscopic and photometric redshifts (see Section 5) we can deduce that almost all these galaxies have $z < 0.5$. Most of the objects then lie reasonably close to the cirrus locus over this redshift range, so we deduce that this bright subset consists of normal spirals with far-infrared emission from interstellar dust bathed in the general stellar radiation field.

Fig. 4 shows the 90–15–6.7 colour–colour diagram for N2 and S1, with the same model loci. Again there is ambiguity about the populations involved, which is not resolved using the fact that most galaxies detected at 90 μm have $z < 0.5$. An earlier version of this figure was discussed by Marquez et al. (2001).

Table 3. Quasar candidates from the blue grens survey of Crampton et al. 1992 that are detected by ELAIS. The name of the sources in the Crampton et al. catalogue and the ELAIS Catalogue are given. This is followed by the separation of the two in arcseconds. The fourth column gives the spectral types estimated from the U, g, r, i, Z INT data in our photometric redshift fitting. The Q flag indicates the confidence of the quasar candidate in the Crampton et al. work from 1 (strong lines) through to 4 (blue continuous spectrum).

Crampton et al. name	ELAIS name	Sepn (arcsec)	opt SED type	Q
1635.20+4124	ELAISC15 J163652.7+411827	1.2	4	2
1635.30+4135	ELAISC15 J163659.0+412928	2.5	6	3
1635.40+4136	ELAISC15 J163702.2+413022	1.1	7	4
1635.70+4121	ELAISC15 J163721.3+411503	0.7	8	3
1636.00+4149	ELAISC15 J163739.3+414348	1.6	7	2
1636.50+4203	ELAISC15 J163805.6+415740	1.4	3	3
1636.70+4133	ELAISR163817+412730	1.3	7	2
1637.20+4217	ELAISC15 J163847.5+421141	0.6	7	4
1637.60+4134	ELAISC15 J163915.9+412834	1.0	6	3
1638.60+4126	ELAISC15 J164016.0+412102	2.5	7	1
1638.70+4108	ELAISC15 J164018.8+410254	1.2	8	3

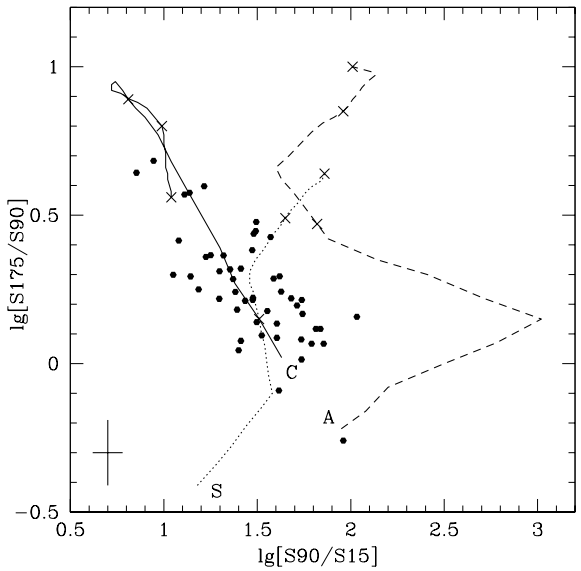

Figure 3. 175–90–15 μm colour–colour diagram for sources in N1 and N2, with loci for cirrus (C), starburst (S) and Arp220 (A) SEDs, from $z = 0$ to $z = 3$ (labels denote the $z = 0$ end of the locus, crosses mark $z = 1$, 2, 3). Only sources detected in all three bands are plotted: all are galaxies. The cross in the lower left-hand corner of this and subsequent figures indicates typical (median) error bars.

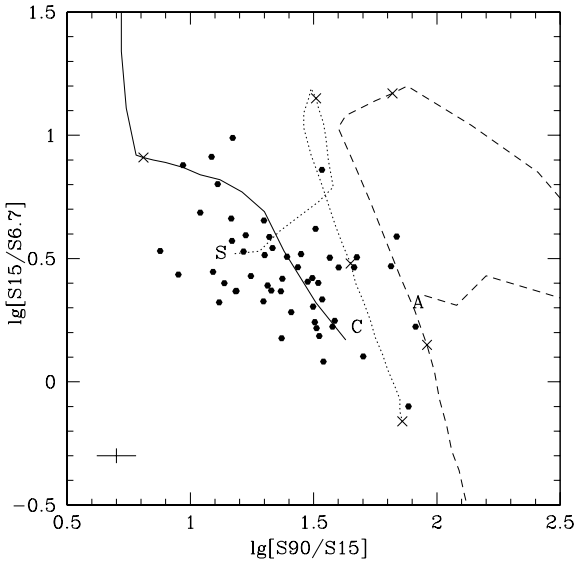

Figure 4. 90–15–6.7 μm colour–colour diagram for sources in N2 and S1 detected in all three bands (all are galaxies), with loci for cirrus (C), starburst (S) and Arp220 (A) SEDs, from $z = 0$ to $z = 3$.

Fig. 5 shows the 90–15–r-band colour–colour diagram for N1, with the same model loci. Here the model loci are more differentiated and we can deduce that all three templates are represented, with cirrus and M82 starburst components accounting for over 75 per cent of the sources.

Optical colours provide a powerful discriminant between galaxies and AGN. Many of the Catalogue sources in N1 and N2 are detected in each of the WFS bands g', r', i'. In Fig. 6 we show the g'–r'–i' colour–colour diagram for sources classified by SExtractor as galaxies. The brighter galaxies define a very tight set of colours, narrower in $(r' - i')$ than in $(g' - r)'$, characteristic of galaxies with $0 < z < 0.5$. Model curves are shown for E, Sbc and starburst galaxies, for $z = 0$–2. In Fig. 7 we show the corresponding plot for objects classified as star-like (excluding actual stars), with different symbols for sources which the photometric redshift code (see Section 5) classifies as having AGN-type SEDs and those with galaxy SEDs. The AGN occupy quite a tight colour region centred on $(g - r) \sim 0.4$, $(r' - i') \sim 0.3$. Model curves are shown for E and starburst galaxies for $z = 0$–2 and for AGN with $z = 0$–6. Objects with galaxy SEDs show some overlap with Fig. 6, but with more scatter to higher values of $(r' - i')$, consistent with having higher redshifts.

Fig. 8 shows $\log(S_{15}/S_r)$ versus $(u - r)$ for ELAIS sources, where S_r denotes the r'-band flux in mJy. There is a clear separation between the Galactic stars in the lower part of the diagram and the AGN and compact galaxies in the upper part, and between the galaxies and AGN. The objects classified as starlike but with galaxy SEDs have values of S_{15}/S_r up to 300 and these must be heavily obscured starbursts like Arp 220, or Type 2 AGN.

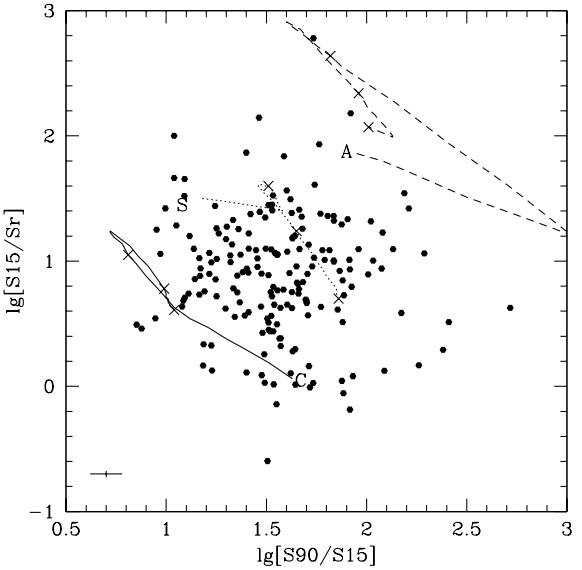

Figure 5. 90–15–r μm colour–colour diagram for N1, N2 and S1, with loci for cirrus (C), starburst (S) and Arp220 (A) SEDs, from $z = 0$ to $z = 3$.

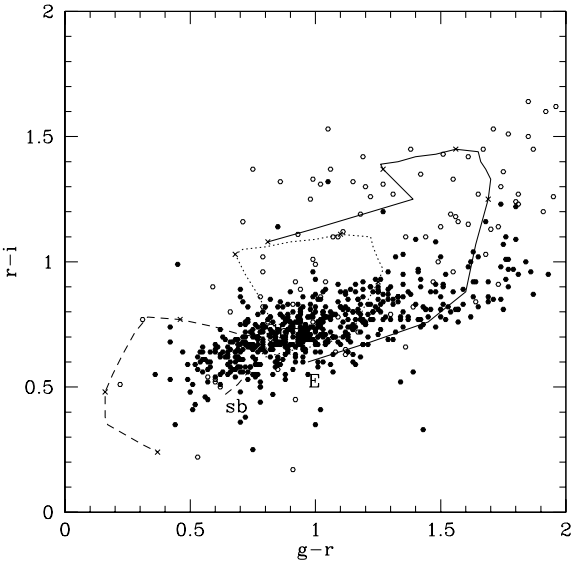

Figure 6. g'–r'–i' colour–colour diagram for galaxies in N1 and N2. Filled circles: $r' < 21$ mag, open circles: $r' > 21$ mag. Model loci for E (solid line), Sbc (dotted line) and starburst (broken line) galaxies are shown for $z = 0$–2 (crosses denote $z = 0.5$, 1, 1.5, 2).

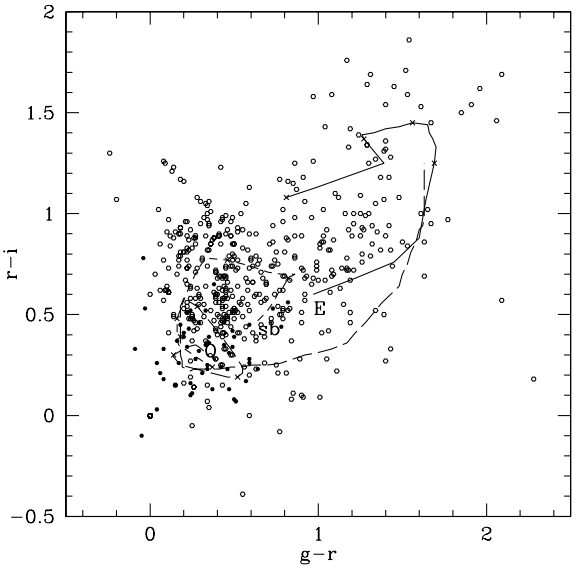

Figure 7. g'–r'–i' colour–colour diagram for star-like objects in N1 and N2. Filled circles: AGN SED, open circles: galaxy SED. Model loci for a quasar (long-dashed line, $z = 0$–6), E galaxy (solid line, $z = 0$–2) and starburst (dashed line, $z = 0$–2), are shown (crosses: $z = 0.5$, 1, 1.5, 2).

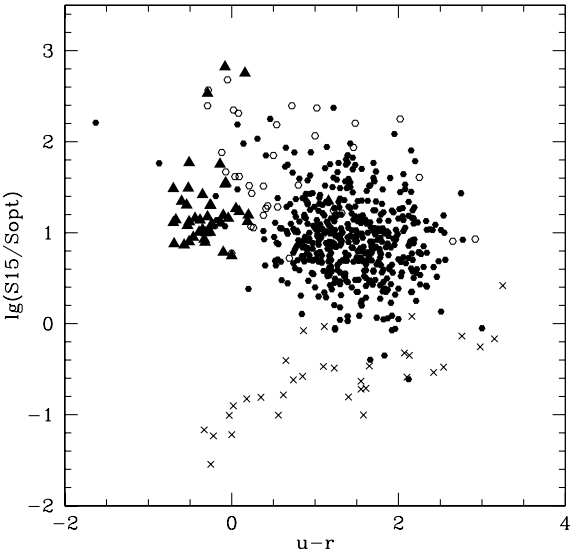

Figure 8. $15/r$ versus $(U - r')$ for ELAIS galaxies and AGN in N1 and N2. Filled circles: extended optical identifications; filled triangles: star-like objects with AGN SEDs; open circles: star-like objects with galaxy SEDs; crosses: Galactic stars. Note that the $(U - r')$ colours of the Galactic stars are inaccurate because of saturation effects.

5 PHOTOMETRIC REDSHIFTS IN N1 AND N2

The WFS optical data in the U, g', r', i', Z bands, and J, H, K data (where available) for N1 and N2 allows us to determine photometric redshifts for a large fraction of the sample. The approach used is that of Rowan-Robinson (2003) with a set of six galaxy templates, and with the option of varying A_V. In addition two simple AGN templates are included, based on the average optical quasi-stellar object (QSO) spectrum of Rowan-Robinson (1995), modified to take account of observed SEDs of ELAIS AGN (details of all the templates used are given at http://astro.ic.ac.uk/∼mrr/photz). Figs 9 and 10 show the comparison of the data for AGN with spectroscopic redshifts with the assumed templates. The application of this code to the full WFS data set is described by Babbedge et al. (2004). We have also used the *UBRI* data in S2 (Pozzi et al. 2003) to estimate photometric redshifts. In S1 we have only *BRI* data in the optical and the photometric calibration at B is uncertain. We found that without U (or u) data, it was impossible to determine photometric redshifts for quasars, but results for galaxies were still good, and these are included in the Catalogue provided at least three photometric bands between B and K are available. Fig. 11 shows the comparison of photometric and spectroscopic redshifts for galaxies in N1, N2, S1 and S2. The spectroscopic redshifts in N1 and N2 are reported by Perez-Fournon et al (in preparation) and Serjeant et al. (2004), in S1 by

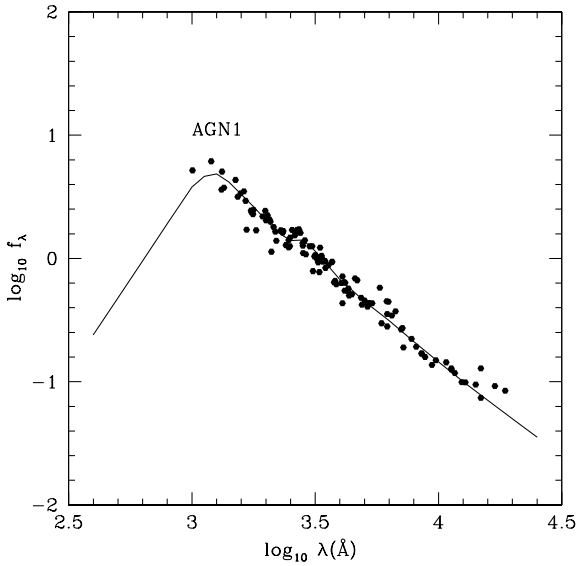

Figure 9. Comparison of photometric data for AGNs with $n_{\rm typ} = 7$ and known spectroscopic redshifts with the assumed template.

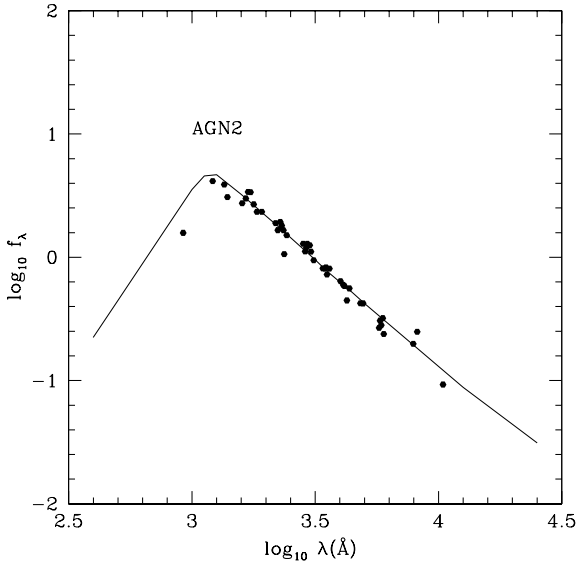

Figure 10. Comparison of photometric data for AGNs with $n_{\rm typ} = 8$ and known spectroscopic redshifts with the assumed template.

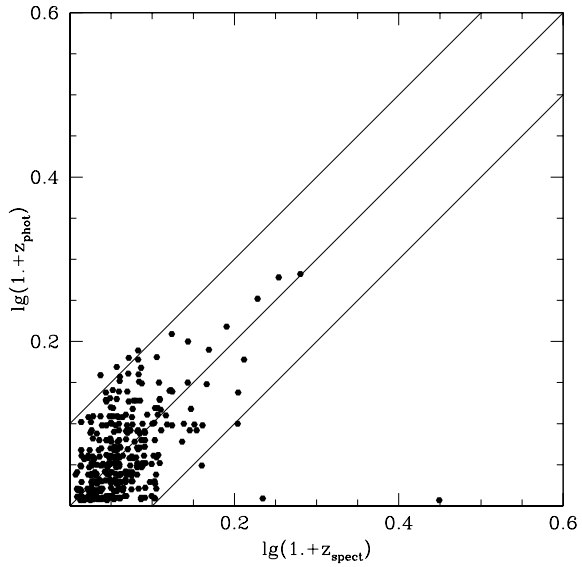

Figure 11. $\log_{10}(1 + z_{\rm phot})$ versus $\log_{10}(1 + z_{\rm spect})$ for galaxies. The straight lines bracket the range $\Delta\log_{10}(1 + z) = \pm0.1$ ($\pm2.5\sigma$ according to the analysis of Rowan-Robinson 2003). The straight lines indicate the $\pm2.5\sigma$ range. The photometric redshifts are for an assumed $A_V = 0$.

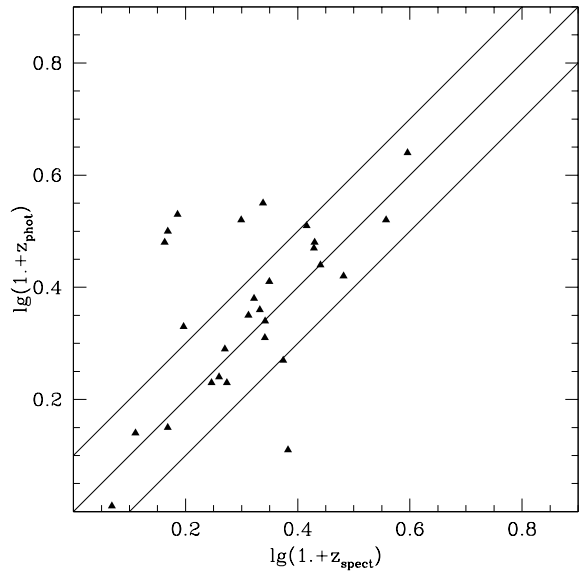

Figure 12. $\log_{10}(1 + z_{\rm phot})$ versus $\log_{10}(1 + z_{\rm spect})$ for AGN.

La Franca et al. (2004) and in S2 by Pozzi et al. (2003). The agreement is good, within the uncertainty of the photometric method ($\sim$10 per cent in $(1 + z)$ according to the analysis of Rowan-Robinson 2003). A fuller discussion of the application of photometric redshift techniques to the WFS data is given by Babbedge et al. (2004). Of course, it needs to be emphasized that a 10 per cent accuracy in $(1 + z)$ means that photometric redshifts $\ll$1 will be very inaccurate. One of the two strongly discrepant points in Fig. 11 is a case where the photometric redshift is determined from only three photometric bands, so as in Rowan-Robinson (2003) we can claim excellent performance for the photometric redshift method if four bands are available. Fig. 12 shows the corresponding plot for AGN in N1, N2 and S2: the results are surprisingly good. Several AGN acquire spurious photometric redshifts in the range 2–2.5 because their *U* magnitudes are fainter than predicted by the template, possibly because of the effect of extinction, so they are interpreted as Lyman drop-outs. The code is quite successful both in finding the AGN and estimating their redshifts. Out of 33 sources with both spectroscopic and photometric redshifts, which are classified either spectroscopically or photometrically as AGN, only two are not classified spectroscopically as AGN, presumably due to aliasing in the photometric solution. Five spectroscopic AGN are not picked up as AGN photometrically though all have consistent photometric redshift estimates, perhaps due a weak AGN continuum. Examples of the template fits to optical and near ir data can be seen in Figs 26–28, later.

Figs 13–16 show redshift histograms at 15, 90 and 175 μm and 20 cm, for sources brighter than the characteristic depth specified in Table 1, with the dotted lines in Figs 11 and 14 indicating

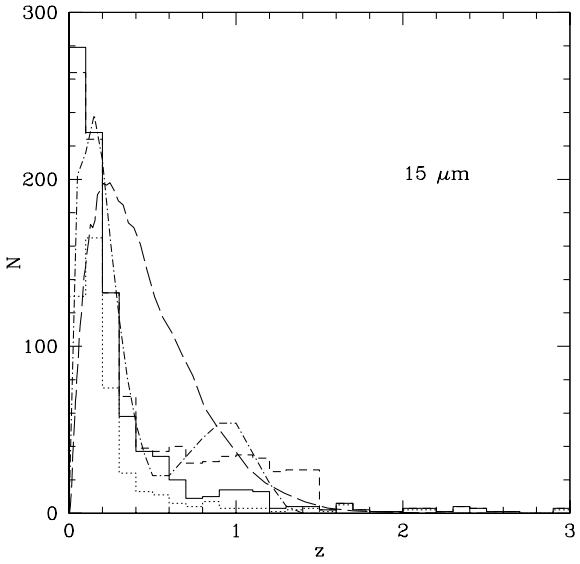

Figure 13. Redshift histogram for ELAIS 15-μm sources. Solid curve: both photometric and spectroscopic redshifts (840 sources); dotted curve: spectroscopic redshifts only (468 sources); broken curve: effect of assigning blank fields uniformly to range $0.5 < z < 1.5$. Long broken curve: predicted redshift distribution from Rowan-Robinson (2001); dash-dotted curve: predicted redshift distribution from Pozzi et al. (2004).

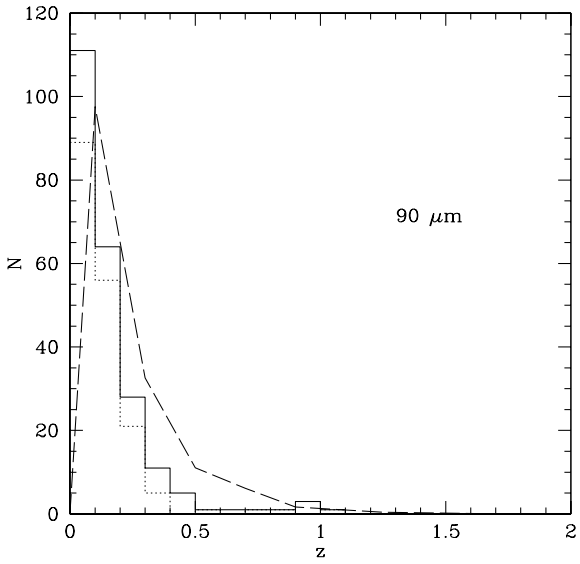

Figure 14. Redshift histogram for ELAIS 90-μm sources. Solid curve: both photometric and spectroscopic redshifts (229 sources); dotted curve: spectroscopic redshifts only (175 sources); long broken curve: predicted redshift distribution from Rowan-Robinson (2001).

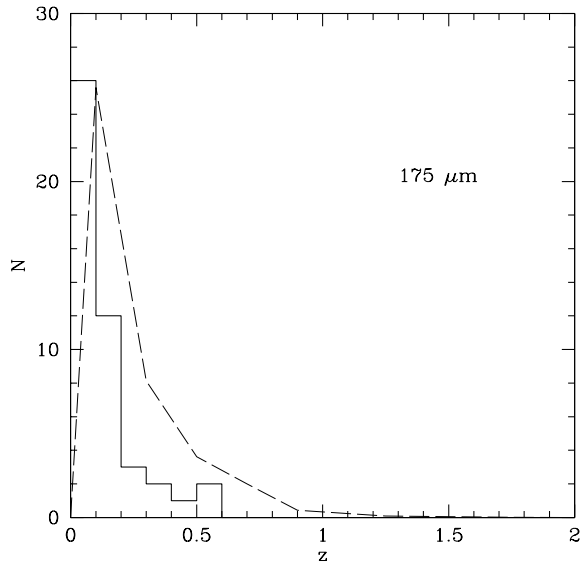

Figure 15. Redshift histogram for ELAIS 175-μm sources. Solid curve: both photometric and spectroscopic redshifts (46 sources). Long broken curve: predicted redshift distribution from Rowan-Robinson (2001).

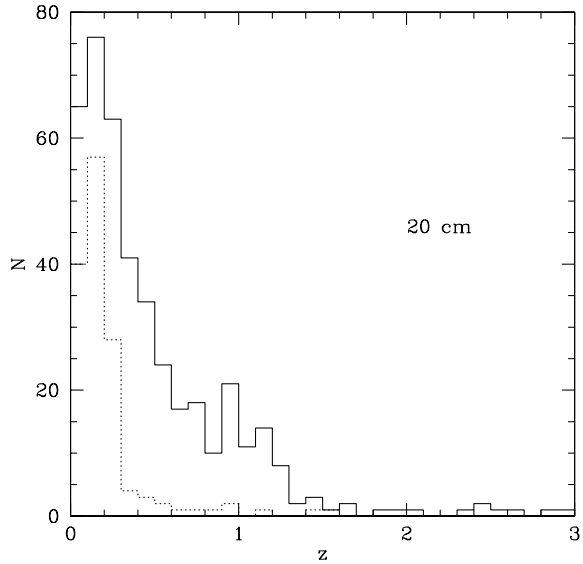

Figure 16. Redshift histogram for ELAIS radio sources. Solid curve: both photometric and spectroscopic redshifts (424 sources); dotted curve: spectroscopic redshifts only (140 sources).

spectroscopic redshifts. The broken histogram indicates the effect of assigning the 15-μm blank-field sources in S1 (which have $R > 20$) redshifts uniformly distributed in the range 0.2–1.5, and the blank-field sources in N1 and N2 (which have $r' > 24$) redshifts uniformly distributed in the range 0.6–1.5, based on the R–z diagram of La Franca et al. (2003, their fig. 15). The median redshift is 0.30 at 20 cm, 0.17 at 15 μm and 0.10 at 90 and 175 μm. In their analysis of the 15-μm redshift distribution in S1, La Franca et al. (2003) and Pozzi et al. (2004) infer a stronger secondary peak at around $z = 1$ than is indicated here. Model predictions by Rowan-Robinson (2001) at 15, 90 and 175 μm are shown in Figs 13–15, and by Pozzi et al. (2003) at 15 μm in Fig. 13. The overall agreement with the Rowan-Robinson (2001) model is reasonable, though the Pozzi et al. (2004) model may be a slightly better fit at 15 μm. This merits further investigation.

The luminosity function and evolution at 15 μm are discussed by La Franca et al. (2004), Perez-Fournon et al. (in preparation), Pozzi et al. (2004), at 90 μm by Serjeant et al. (2004) and at 175 μm by Perez-Fournon et al. (in preparation).

Fig. 17 shows $\log(S_{15}/S_r)$ versus z, where $z = z_{\rm best}$, for objects classified by SExtractor as galaxies, together with predicted loci for cirrus, M82 and Arp220 starbursts. Although most of the galaxies have $z < 0.3$, there is an interesting subset with $0.6 < z < 1.2$. Fig. 18

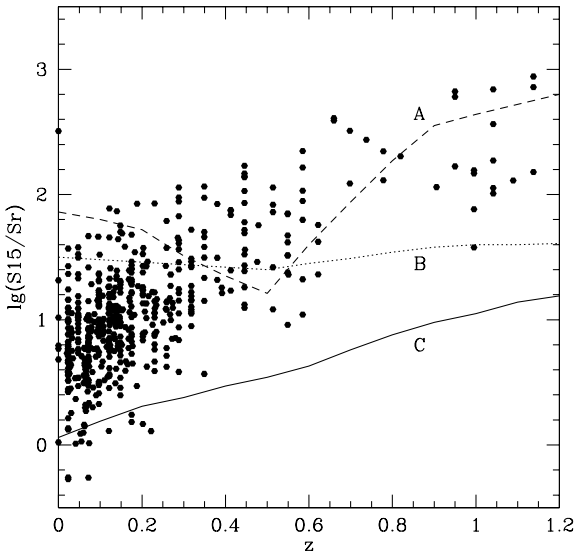

Figure 17. 15-μm/*r*-band colour versus z for ELAIS galaxies, with loci for cirrus (C, solid line), starburst (B, dotted line) and Arp220 (A, broken line) SEDs.

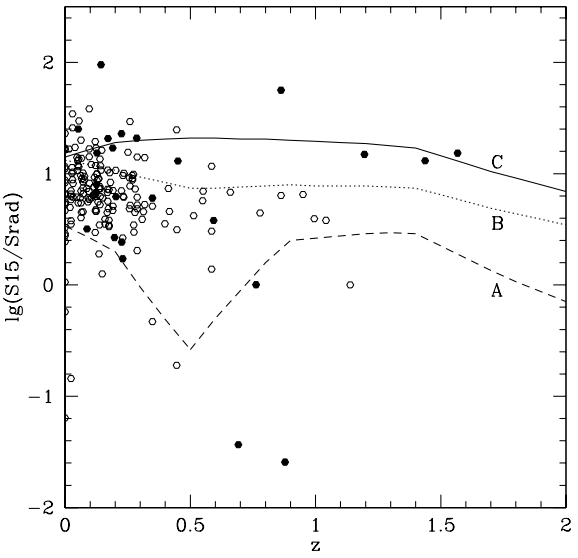

Figure 19. 15-μm/20-cm colour versus z for ELAIS Catalogue sources, with loci for cirrus (C, solid line), starburst (B, dotted line) and Arp220 (A, broken line) SEDs. Filled circles: AGN; open circles: galaxies.

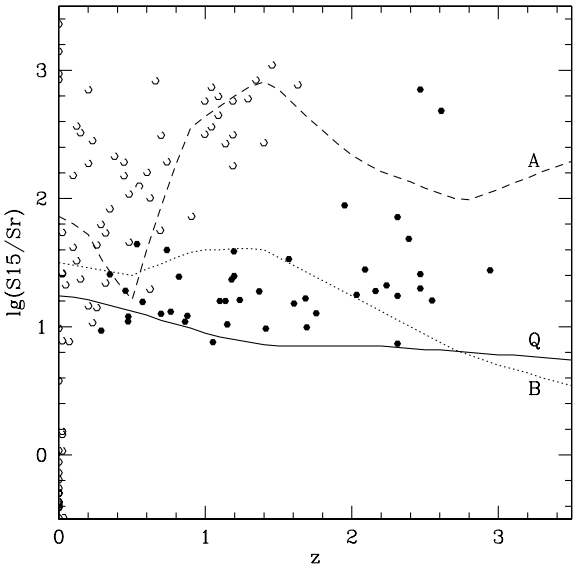

Figure 18. 15-μm/*r*-band colour versus z for ELAIS star-like sources (excluding stars), with loci for AGN (Q, solid line), starburst (B, dotted line) and Arp220 (A, broken line) SEDs. Filled circles: sources with AGN optical SEDs; open circles: sources with galaxy SEDs.

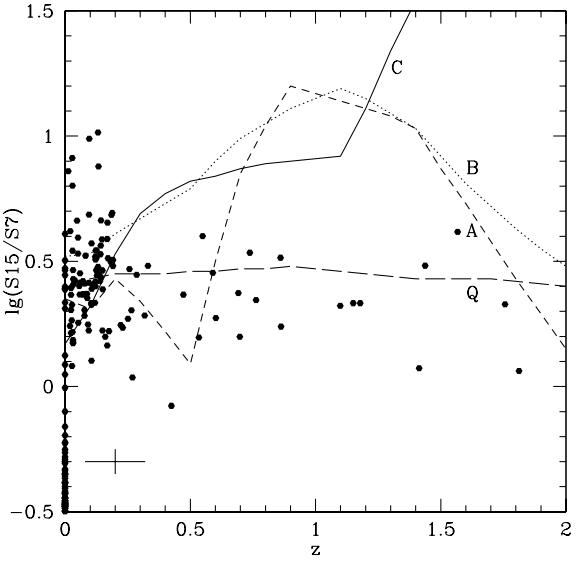

Figure 20. 15/6.7-μm, colour versus z for N2 and S1, with loci for cirrus (C, solid line), starburst (B, dotted line), Arp220 (A, short broken line) and AGN dust tori (Q, long broken line) SEDs.

shows the corresponding diagram for star-like objects, with model loci for AGN dust tori, and M82 and Arp220 starbursts. The objects with AGN SEDs, shown as filled circles, follow the (Type 1) AGN dust torus model line well. Most with galaxy SEDs (and some from Fig. 17 with $0.2 < z < 0.8$) have S_{15}/S_r values higher than any of the model loci. These may represent a new population of heavily obscured starbursts or Type 2 AGN.

Fig. 19 shows $\log(S_{15}/S_{20\,\mathrm{cm}})$ versus z for all sources, for an assumed rest-frame $S_{60}/S_{20\,\mathrm{cm}}$ ratio of 200. There is a dependence of $S_{15}/S_{20\,\mathrm{cm}}$ on infrared SED type and on redshift. Thus even if there is a perfect correlation between 60-μm and 20-cm flux, we do not expect this correlation to be preserved at other infrared wavelengths. Note the two radio-loud AGN in the lower part of Fig. 19. The 15-μm–radio correlation has also been discussed by Gruppioni et al. (2003).

Fig. 20 shows $\log(S_{15}/S_{6.7})$ versus redshift for all sources in N2 and S1. Values of $S_{15}/S_{6.7} < 1$ are predominantly stars and have been correctly recognized as such by the photometric redshift code. The 15/6.7 colour ratio is not a good discriminant between the galaxy models at low redshift, though it is clear that at high redshift the sources conform well to the AGN dust torus locus.

Figs 21 and 22 show $\log(S_{90}/S_r)$ and $\log(S_{175}/S_r)$ versus z, with model loci for cirrus, M82 and Arp220 starbursts. The models nicely bracket the observational points. However a plot of $\log(S_{175}/S_{90})$ versus $\log(1+z)$ (Fig. 23) shows that at low redshifts there is a group of nearby galaxies with colder dust [$\nu B_\nu(T)$ colour temperatures in the range 18–25 K] than the cirrus template used here

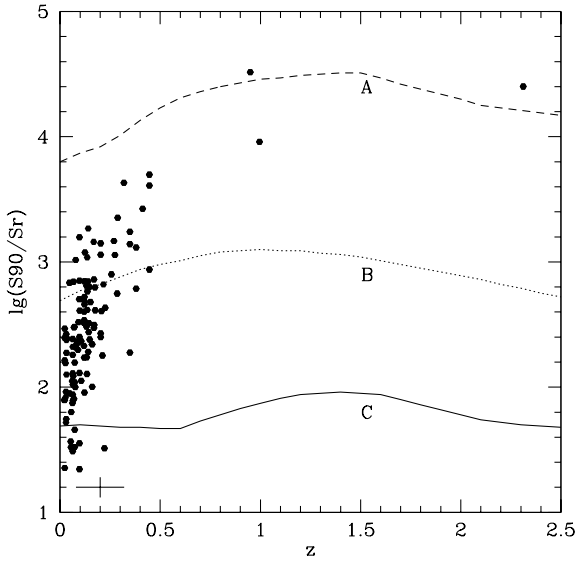

Figure 21. 90-μm/r-band colour versus z for ELAIS galaxies, with loci for cirrus (C, solid line), starburst (B, dotted line) and Arp220 (A, broken line) SEDs.

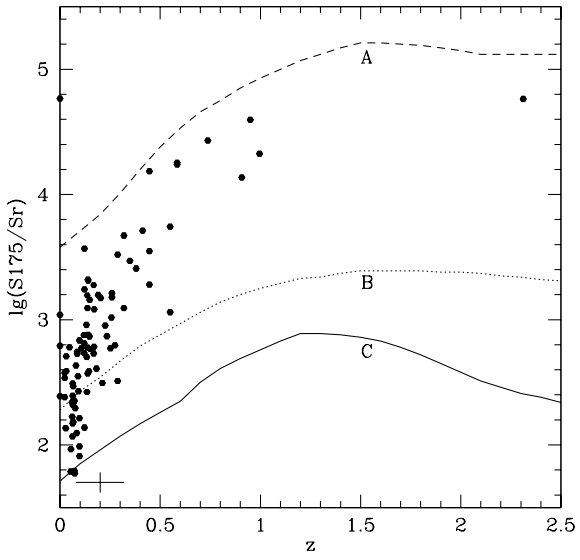

Figure 22. 175-μm/r-band colour versus z for galaxies in N1 and N2, with loci for cirrus (C, solid line), starburst (B, dotted line) and Arp220 (A, broken line) SEDs.

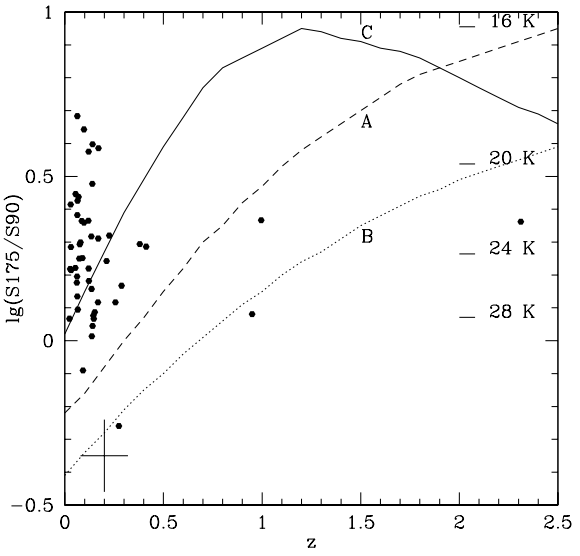

Figure 23. 175/90-μm, colour versus z for galaxies in N1 and N2, with loci for cirrus (C, solid line), starburst (B, dotted line) and Arp220 (A, broken line) SEDs. Horizontal bars at right indicate dust colour temperatures from a $\nu B_\nu(T)$ model.

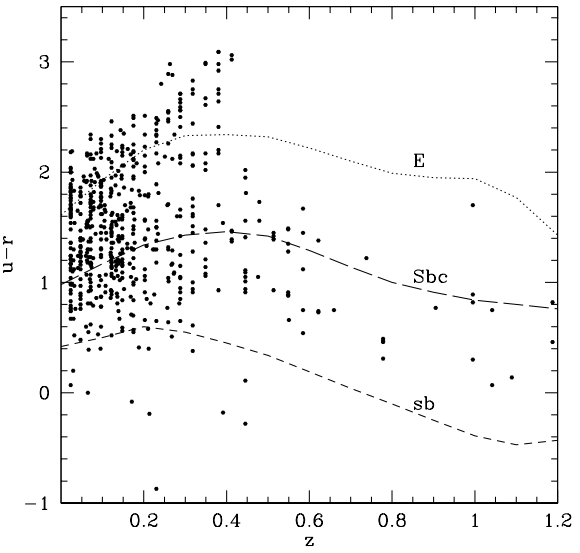

Figure 24. $U - r'$ versus z for galaxies in N1 and N2. Model loci are for an E galaxy (dotted line), Sbc galaxy (long-dashed line) and starburst (dashed line).

(which matches *IRAS* colours for cirrus sources well). Clearly we do not expect all the dust in a galaxy to be at a single temperature. As we move to longer wavelengths we expect to see emission from cooler dust further from the centre of the galaxy. Observations of these galaxies at 350–850 μm would be valuable for understanding the true distribution of dust mass and temperature in galaxies.

Fig. 24 shows $(u - r)$ versus $\log_{10}(1 + z)$ for objects classified as extended, compared with model predictions for E, Sbc and starburst galaxy SEDs. The photometric redshift code suggests that galaxies with $(u - r) > 2$ show evidence of extinction, with A_V in the range 1–3. Fig. 25 shows the corresponding diagram for star-like objects. The objects with AGN-type SEDs follow a narrow locus, with objects with spectroscopic redshifts (filled circles) agreeing well with the adopted AGN SED, while those with galaxy SEDs occupy a similar region to the galaxies of Fig. 24.

A full discussion of the *JHK*, 6.7- and 15-μm colour–colour diagrams has been given by Vaisanen et al. (2002) and the results are not significantly altered by the larger and more accurately calibrated sample here. The *JHK* data help the photometric redshift fitting but do not help us to understand the nature of the dust-emission components in galaxies.

6 INFRARED SPECTRAL ENERGY DISTRIBUTIONS

For sources detected in multiple *ISO* bands we can compare the infrared spectral energy distributions with those for standard model

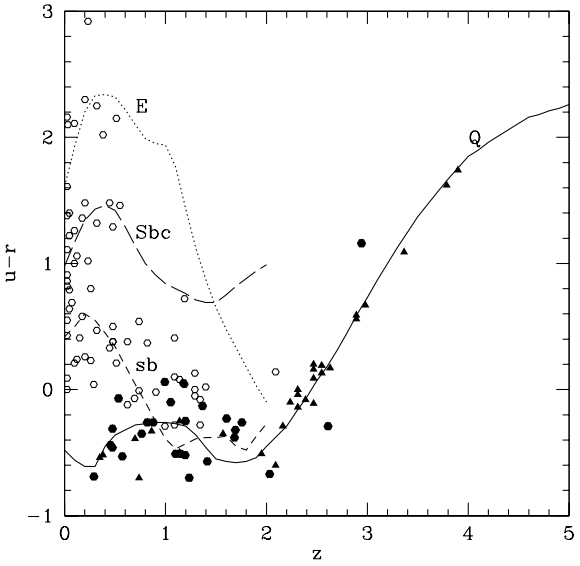

Figure 25. $U - r'$ colour versus z for star-like objects in N1 and N2. Filled triangles denote objects with AGN SEDs, filled circles are spectroscopic AGN (Sy 1 and 2) and open circles are objects with galaxy SEDs. The model loci are for an AGN (solid line), E galaxy (dotted line), Sbc galaxy (long-dashed line) and starburst (dashed line).

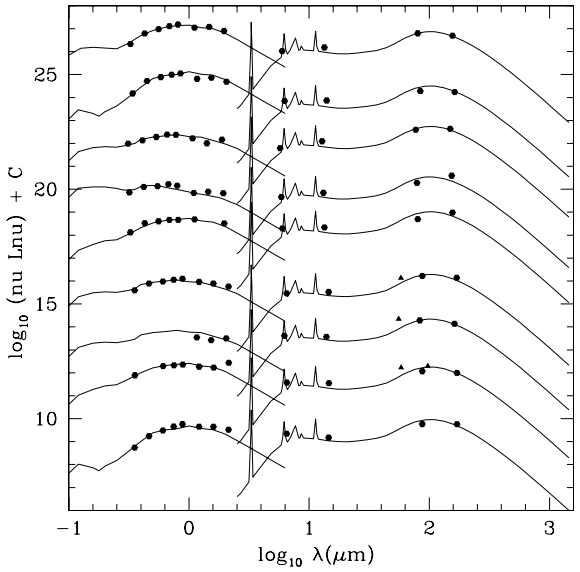

Figure 26. Nine ELAIS galaxies detected in all four *ISO* bands for which a standard cirrus model provides an excellent fit to the spectral energy distribution. Filled circles: *ISO* data; filled triangles: *IRAS* data. From bottom: ELAISC15 163359.2+405303 ($L_{\rm ir}$ = 10.13, $n_{\rm typ}$ = 1), 163401.8+412052 (10.42, 3), 163506.1+411038 (11.01, 4), 163525.1+405542 (10.46, 4), 163546.9+403903 (11.19, 3), 163548.0+412819 (11.21, 5), 163607.7+405546 (11.41, 4), 163613.6+404230 (10.67, 1), 163641.1+413131 (11.04, 2).

templates. Fig. 26 compares the rest-frame SEDs of nine galaxies detected in all four *ISO* bands with a standard cirrus emission spectrum (Efstathiou & Rowan-Robinson 2003: surface brightness parameter $\psi = 5$, age of starburst = 5 Gyr). All have modest infrared luminosities ($L_{\rm ir} < 11.5$). Fig. 27 shows a similar plot for luminous cirrus galaxies ($L_{\rm ir} > 11.5$). These represent an interesting new population of luminous cool galaxies, with redshifts in the range 0.15–0.5,

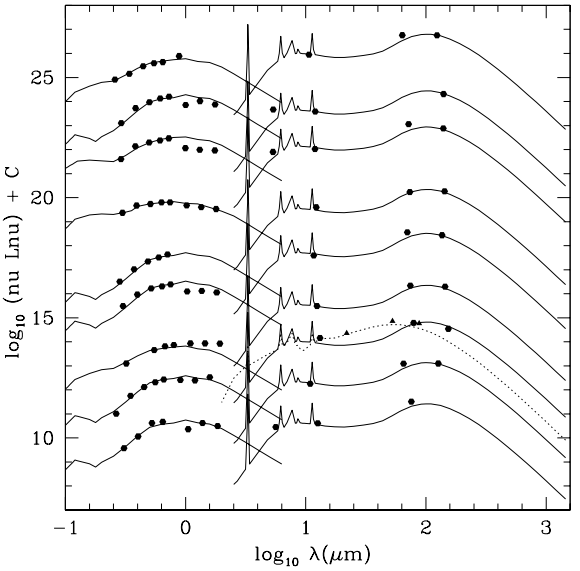

Figure 27. Nine luminous ELAIS galaxies detected in three *ISO* bands for which a standard cirrus model provides an excellent fit to the spectral energy distribution. Filled circles: *ISO* data; filled triangles: *IRAS* data. From bottom: ELAISC15 050225−3041112 ($L_{\rm ir}$ = 11.59, $n_{\rm typ}$ = 1), 160443.5+543332 (12.30, 1), 160552.5+540650 (11.99, 3), 160553.3+542225 (11.52, 1), 160945.7+534944 (11.68, 1), 161041.2+541032 (11.51, 4), 163242.4+410847 (12.11, 2), 163449.5+412048 (11.61, 1), 163741.3+4111913 (11.97, 3). An additional starburst component is shown for 160552.5+540650 (dotted curve).

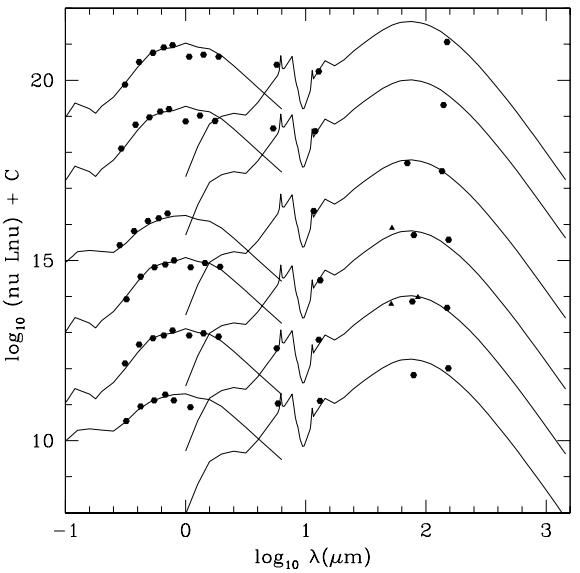

Figure 28. Six ELAIS galaxies detected in three or four *ISO* bands for which an Arp200 model provides an excellent fit to the spectral energy distribution. From bottom: 163412.0+405652 (11.40, 2), 163608.1+410507 (12.16, 1), 160934.7+53220 (11.46, 1), 161300.8+544838 (11.98, 2), 163449.5+412048 (12.15, 1), 163708.1+412856 (11.77, 1).

consistent with the strong evolution postulated for cirrus galaxies by Rowan-Robinson (2001) and perhaps related to the very luminous cirrus galaxies postulated by Efstathiou & Rowan-Robinson (2003) to explain some of the high-redshift SCUBA galaxies. For 160552.5+540650 there is evidence also for a starburst component. Fig. 28 compares two galaxies detected in four *ISO* bands

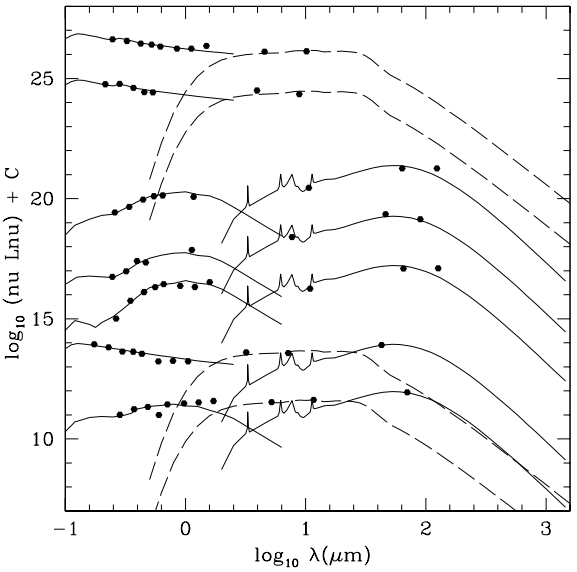

Figure 29. Five ELAIS galaxies detected in three *ISO* bands compared with an M82 starburst model. For two of the galaxies an AGN dust torus component has been included to fit the mid-ir data (model from Rowan-Robinson 1995). The top two loci are sources identified with quasars, with evidence only for dust torus emission in the infrared. From bottom: ELAIS 163751.4+413027 (12.20, 4), 164010.1+410521 (13.17, 8), 160443.5+543332 (12.41, 1), 163615.7+404759 (13.00, 2), 163741.3+411913 (12.11, 3), 163352.4+402112 (11.79, 7), 163502.7+412953 (11.48, 7).

and four detected in three *ISO* bands with a high optical-depth starburst model which gives a good fit to Arp 220 (Efstathiou et al. 2000a: $A_V = 200$, age of starburst = 26 Myr). They tend to have higher infrared luminosities and optical SED type $n_{\rm typ} = 1$ or 2 (E or Sab), consistent with the optical SED of Arp220, which shows very little contribution from young massive stars due to the high extinction in this galaxy. Fig. 29 compares three galaxies detected in three *ISO* bands with an M82-type starburst model (Efstathiou et al. 2000a: $A_V = 50$, age of starburst = 26 Myr). Two galaxies for which an AGN dust torus component is also required are included, as well as a further two objects which only require an AGN dust torus component. These figures include all ultraluminous ELAIS galaxies detected in three bands ($L_{\rm ir} > 12.22$). The four infrared SED model components used in Figs 26–29 are the same as those used in count models by Rowan-Robinson (2001).

For all ELAIS galaxies detected in two or more bands and with spectroscopic or photometric redshifts (a total of 306 galaxies) we have selected the best-fitting of the four model components cirrus, M82, Arp220 and AGN dust torus, and estimated the bolometric infrared luminosity (from 3 to 1000 μm: here L denotes the $\log_{10}$ of the luminosity). We have used the 15-μm flux (or upper limit) to estimate the luminosity in an AGN dust torus component, $L_{\rm tor}$, if the 15-μm emission is interpreted as due to such a component (without corroboration at longer wavelengths, $L_{\rm tor}$ gives a more conservative estimate of luminosity than starburst or cirrus models). We estimated the corresponding optical bolometric luminosities (0.04–3 μm), using the photometric SED templates (Rowan-Robinson 2003). Fig. 30 shows a plot of $(L_{\rm ir} - L_{\rm opt})$ versus $L_{\rm ir}$. For ease of comparison with

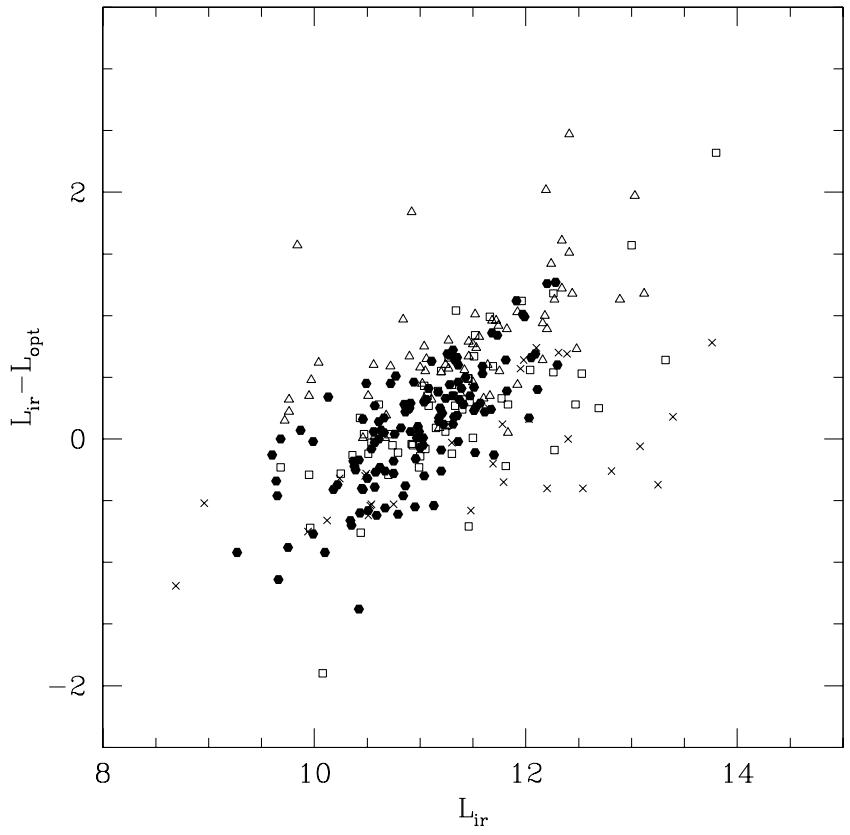

Figure 30. $L_{\rm ir} - L_{\rm opt}$ versus $L_{\rm ir}$ for ELAIS galaxies detected in two or more *ISO* bands and with spectroscopic or photometric redshifts. Filled circles: cirrus SED; open squares: M82 starburst; open triangles: Arp 220 starbursts; crosses: M82 starburst+AGN dust torus.

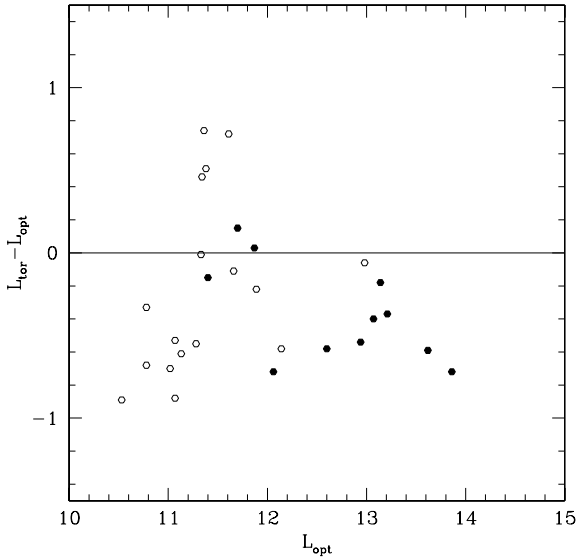

Figure 31. $L_{ir} - L_{opt}$ versus L_{ir} for ELAIS AGN dust tori detected in two or more *ISO* bands and with spectroscopic or photometric redshifts. Filled circles: Sy 1 (from optical spectroscopy), open circles: Sy 2, or galaxy SED in optical.

earlier work, an Einstein–de Sitter model ($\Omega = 1$, $\Lambda = 0$), with $H_0 = 50$, is used.

Galaxies with lower L_{ir} and $L_{ir} - L_{opt} < 0.0$ are predominantly fitted with cirrus models, but cirrus models are also required at higher luminosities and values of $L_{ir} - L_{opt}$ as high as 1.0. This would seem to be consistent with the concept discussed by Efstathiou & Rowan-Robinson (2003) of cirrus galaxies with $1 < A_V < 3$ and high total luminosities, as an alternative explanation of many of the galaxies detected in submillimetre surveys. It is also consistent with the source-count models of Rowan-Robinson (2001), in which the quiescent, cirrus galaxy component undergoes the same strong luminosity evolution as starburst galaxies. This high incidence of cold, very luminous, galaxies with high infrared-to-optical ratios is one of the main new results of the ELAIS survey. The expected trend towards M82- and Arp220-type infrared SEDs as we go to higher infrared luminosities and higher values of $L_{ir} - L_{opt}$ is also clearly seen.

Fig. 31 shows a similar plot for galaxies for which an AGN dust torus component is preferred. Where galaxies are detected only at 6.7 and 15 μm, and starburst luminosities in the hyperluminous range are implied, we have always preferred a dust torus model as the more conservative assumption. For Type 1 AGN, $L_{ir} - L_{opt}$ can be interpreted as the log of the covering factor. The observed values are in the range −0.7 to 0, implying covering factors in the range 20–100 per cent, with a median value of 30 per cent. Values greater than 0 would imply that the optical QSO must have suffered some extinction.

7 ULTRALUMINOUS AND HYPERLUMINOUS INFRARED GALAXIES

We have found a surprisingly large population of Arp220-like ultraluminous infrared galaxies ($L_{ir} > 12.22$) in this survey (14 per cent of the 15-μm galaxies with known z). Morel et al. (2001) reported the first hyperluminous infrared galaxy in the survey. In fact there are a total of nine candidate hyperluminous galaxies ($L_{ir} > 13.22$, Rowan-Robinson 2000) in the survey, listed in Table 4 (note that for galaxies ir SED-type = 6, the luminosity in the starburst and AGN dust torus components must be added to get the total infrared luminosity). A further 45 galaxies would be hyperluminous if their 15-μm emission were interpreted as due to a starburst SED (rather than the more conservative assumption that it is due to AGN dust torus emission). All nine objects in Table 4 appear to be quasars: selection at 15 μm does favour detection of AGN dust tori. For four galaxies this classification is based only on a photometric redshift, and this needs to be confirmed by spectroscopy (especially where $z_{ph} = 2$–2.5, since there is a strong possibility of aliasing – see Section 5). The large number of ultraluminous and hyperluminous infrared galaxies is probably a reflection of the very steep rise in the star formation rate between $z = 0$ and $z = 2$, and the associated strong evolution in the AGN population (cf. La Franca et al. 2003; Pozzi et al. 2003), though gravitational lensing could also play a part.

We also find nine extremely red objects (EROs) in the survey, defined as $(r - K) > 6$, all from the K-band photometry of Vaisanen et al. (2002) and Rigopoulou et al. (in preparation), and these are listed in Table 5. Three of the objects have photometric redshifts and have the SEDs of elliptical galaxies at a redshift ∼1. Predicted $(r - K)$ colours as a function of z show that elliptical galaxies have values >6 for $1 < z < 4$,

In the optical and near-infrared the SEDs of dusty starbursts like M82 and Arp 220 look very like ellipticals due to the extinction of the young stellar component. Table 5 gives the values of $\log_{10}(S_{15}/S_r)$ and $\log_{10}(S_{rad}/S_r)$, which are consistent with all nine objects being highly extinguished starbursts like Arp 220, at $z \sim 1$ (cf. Arp 220 model curves in Figs 16 and 17). However only a small fraction of EROs will fall into this category of highly extinguished starbursts. None of the 17 EROs with $(R - K) > 6$ in table 2 of Roche et al. (2002), which are located within a small 81.5 arcmin^2 area of N2, are

Table 4. Hyperluminous infrared galaxies in the ELAIS Catalogue.

Name	m_r	f_{WFS}	n_{typ}	z_{ph}	z_{spect}	n_{ztyp}	n_{zref}	L_{opt}	n_{ISO}	n_{irtyp}	L_{ir}	L_{tor}
ELAISC15-J002925-434917	18.63	–	–	–	3.094	5	3	13.59	1	2	14.80	13.54
ELAISC15-J003213-434553	17.09	–	–	–	1.707	5	3	13.57	1	2	13.97	13.29
ELAISC15-J050152-303519	17.86	–	4	0.0233	1.813	5	4	13.62	2	4	13.25	13.07
ELAISC15-J160419.0+541524	18.00	0.99	8	2.548	–	–	–	13.42	1	2	14.51	13.39
ELAISR 160758+542353	22.70	0.10	8	2.311	–	–	–	11.48	2	2	13.80	−12.57
ELAISC15-J161259.2+541505	19.06	0.98	8	2.548	–	–	–	12.98	2	6	13.76	13.03
ELAISC15-J163739.2+405643	–	–	–	–	1.438	5	1	–	3	2	13.42	12.67
ELAISC15-J164010.1+410521	16.95	1.00	8	1.399	1.0990	5	6	13.17	3	6	13.39	12.92
ELAISC15-J164018.4+405812	18.06	0.99	8	2.311	–	–	–	13.33	1	2	14.33	13.30

Table 5. EROs in the ELAIS catalogue.

Name	r'	K	$n_{\rm typ}$	$z_{\rm phot}$	$\log(S_{15}/S_r)$	$\log(S_{\rm rad}/S_r)$
ELAISR160721+544757	24.11	18.076	–	–	–	3.60
ELAISC15−J160913.2+542320	24.29	17.180	–	–	3.48	–
ELAISR161030+540247	23.53	16.400	–	–	–	2.91
ELAISR161046+542329	23.15	17.090	2	1.138	–	2.28
ELAISC15−J163536.6+404754	23.38	17.340	1	0.995	2.71	–
ELAISR163555+412233	23.29	16.789	1	1.291	2.62	–
ELAISR163723+410526	23.71	17.449	–	–	–	3.33
ELAISC15−J163748.1+412100	24.50	17.926	–	–	3.14	–
ELAISR163758+411741	23.79	17.413	–	–	–	2.32

detected by *ISO* (one is an ELAIS radio source, 163657+410021). Counts of EROs in the N1 and N2 areas, and estimates of their space density, are given by Vaisanen & Johansson (2004). They conclude that the redshifts of their ERO sample lie in the range 0-7–1.5 and estimate the fraction of strong starbursts ($>30\,M_o\,{\rm yr}^{-1}$) to be <10 per cent.

8 DISCUSSION AND CONCLUSIONS

We have presented the Final ELAIS Catalogue at $U, g', r', i', Z, J, H, K$, 6.7, 15, 90 and 175 μm, and 20 cm. The process of band-merging and optical association of the sources has given considerable insight into the extragalactic infrared populations present. Although the largest single population is relatively nearby ($z < 0.2$) cirrus galaxies, there is a surprisingly large population of ultraluminous infrared galaxies (14 per cent of 15-μm galaxies), many of them highly obscured starbursts like Arp 220. There is also a significant population of luminous ($L_{\rm ir} > 11.5$) cool galaxies, consistent with the idea that the quiescent component of star formation in galaxies undergoes the same strong evolution as the starburst component. There appear to be a small proportion of genuinely optically blank fields to $r' = 24$ (10 per cent at 15 μm, 3 per cent at 6.7 μm, up to 20 per cent at 90 μm, and 1 per cent at 175 μm) which must have high infrared-to-optical ratios, be at higher redshift ($z > 0.6$), and have high infrared luminosities. They are therefore dusty luminous starbursts or Type 2 AGN.

The ELAIS survey provides a strong basis for the SIRTF surveys. The SWIRE Legacy Survey will include the ELAIS N1, N2, and S1 areas. It will be worthwhile to obtain better SEDs and ir spectroscopy for the luminous infrared galaxies in the survey. As SIRTF does not have a 15-μm band, the ELAIS data will be a useful complement to the SWIRE data. The results presented here illustrate the importance of multiband optical data for photometric redshift determination. The far-infrared colour–colour diagrams discussed here illustrate the difficulties of trying to determine redshifts from far-infrared data alone.

ACKNOWLEDGMENTS

The ELAIS consortium acknowledges support from EC TMR Networks '*ISO* Survey' and 'POE', and from PPARC. DMA and OA acknowledge support from the Royal Society. We thank the referee for helpful suggestions which have improved this paper.

REFERENCES

Alexander D. M. et al., 2001, ApJ, 554, 18
Babbedge T., 2004, PhD thesis, Univ. London
Babbedge T. et al., 2004, MNRAS, submitted
Basilakos S. et al., 2002, MNRAS, 331, 417
Blommaert J. et al., 1998, ISOCAM Handbook. Available online at http://www.iso.vilspa.esa.es/manuals/HANDBOOK/cam_hb/
Chapman S. C., Smail I., Ivison R. J., Helou G., Dale D. A., Lagache G., 2002, ApJ, 573, 66
Ciliegi P. et al., 1999, MNRAS, 302, 222
Cram L., Hopkins A., Mobasher B., Rowan-Robinson M., 1998, ApJ, 507, 155
Crampton D., Cowley A. P., Hartwick F. D. A., Ko P. W., 1992, AJ, 104, 1706
Dole H. et al., 2001, A& A, 372, 364
Efstathiou A., Rowan-Robinson M., 2003, MNRAS, 343, 322
Efstathiou A., Rowan-Robinson M., Siebenmorgen R., 2000a, MNRAS, 313, 734
Efstathiou A. et al., 2000b, MNRAS, 319, 1169
Goldschmidt P. et al., 1997, MNRAS, 289, 465
Gonzalez-Solares E. et al., 2004, MNRAS, submitted (astro-ph/0402406)
Gruppioni C. et al., 1999, MNRAS, 305, 297
Gruppioni C., Lari C., Pozzi F., Zamorani G., Franceschini A., Oliver S., Rowan-Robinson M., Serjeant S., 2002, MNRAS, 335, 831
Gruppioni C., Pozzi F., Zamorani G., Ciliegi P., Lari C., Calabrese E., La Franca F., Matute I., 2003, MNRAS, 341, L1
Héraudeau P. et al., 2004, MNRAS, submitted
Hughes D. H. et al., 1998, Nat, 394, 241
La Franca F. et al., 2004, AJ, in press (astro-ph/0403211)
Lari C. et al., 2001, MNRAS, 325, 1173
Lonsdale C. et al., 2003, PASP, 115, 897
Mann R. G. et al., 1997, MNRAS, 289, 482
Mann R. G. et al., 2002, MNRAS, 332, 549
Manners J. C. et al., 2003, MNRAS, 343, 293
Marquez I. et al., 2001, in Pilbratt G. L., Cernicharo J., Heras A. M., Prusti T., Harris R., eds, Proc. ESA SP-460, The Promise of the Herschel Space Observatory. ESA Publications Division, Noordwijk, p. 147
Matute I. et al., 2002, MNRAS, 332, L11
Moshir M., Kopman G., Conrow T. A. D., 1992, IRAS Faint Source Survey, Explanatory Supplement, version 2. IPAC, California Institute of Technology, Pasadena
Morel T. et al., 2001, MNRAS, 327, 1187
Oliver S. et al., 1997, MNRAS, 289, 471
Oliver S. et al., 2000, MNRAS, 316, 768
Oliver S. et al., 2002, MNRAS, 332, 536
Pascual S., Gallego J., Aragon-Salamanca A., Zamorano J., 2001, A& A, 379, 798
Pozzi F. et al., 2003, MNRAS, 343, 1348
Pozzi F., Gruppioni C., Oliver S., Matute I., La Franca F., Lari C., Zamorani G., Rowan-Robinson M., 2004, ApJ, accepted (astro-ph/0403242)
Roche N. D., Almaini O., Dunlop J., Ivison R. J., Wilcox C. J., 2002, MNRAS, 337, 1282
Rowan-Robinson M., 1995, MNRAS, 272, 737

Rowan-Robinson M., 2000, MNRAS, 316, 885
Rowan-Robinson M., 2001, ApJ, 549, 745
Rowan-Robinson M., 2003, MNRAS, 345, 819
Rowan-Robinson M., Efstathiou A., 1993, MNRAS, 263, 675
Rowan-Robinson M. et al., 1997, MNRAS, 289, 490
Rowan-Robinson M., et al., 1999, in Cox P., Kessler M. F., eds, ESA-SP 427, The Universe as seen by ISO. ESA Publications, Noordwijk, p. 1011
Sajina A., Borys C., Chapman S., Dole H., Halpern M., Lagache G., Puget J.-L., Scott D., 2003, MNRAS, 343, 1365
Serjeant S. et al., 1997, MNRAS, 289, 457
Serjeant S. et al., 2000, MNRAS, 316, 768
Serjeant S. et al., 2001, MNRAS, 322, 262
Serjeant S. et al., 2004, MNRAS, submitted, (astro-ph/0401289)
Vaccari M. et al., 2004, MNRAS, submitted (astro-ph/0404315)
Vaisanen P., Johansson P. H., 2004, A&A, submitted
Vaisanen P. et al., 2002, MNRAS, 337, 1043
Willott C. J. et al., 2003, MNRAS, 339, 397

This paper has been typeset from a TEX/LATEX file prepared by the author.